Cell size modulates ferroptosis susceptibility

Evgeny Zatulovskiy[1,2,*], Magdalena B. Murray[2], Shuyuan Zhang[2], Scott J. Dixon[2], Jan M. Skotheim[2,3,*]

[1] Department of Biochemistry, University of Cambridge, Cambridge, CB2 1GA, UK

[2] Department of Biology, Stanford University, Stanford, CA 94305, USA

[3] Chan-Zuckerberg Biohub, Stanford, CA 94305, USA

* Correspondence: ez225@cam.ac.uk (E.Z.), skotheim@stanford.edu (J.M.S.)

ABSTRACT

Size is a fundamental property of cells that influences many aspects of their physiology. This is because cell size sets the scale for all subcellular components and drives changes in the composition of the proteome. Given that large and small cells differ in their biochemical composition, we hypothesize that they should also differ in how they respond to signals and make decisions. Here, we investigated how cell size affects susceptibility to cell death. We found that large cells are more resistant to ferroptosis caused by system x_c^- inhibition. Ferroptosis is a type of cell death characterized by the iron-dependent accumulation of toxic lipid peroxides. This process is opposed by cysteine-dependent lipid peroxide detoxification mechanisms. We found that larger cells exhibit higher concentrations of the cysteine-containing metabolite glutathione and lower concentrations of membrane lipid peroxides. Mechanistically, this can be explained by the fact that larger cells had lower concentrations of an enzyme that enriches cellular membranes with peroxidation-prone polyunsaturated fatty acids, ACSL4, and increased concentrations of the iron-chelating protein ferritin, the glutathione-producing enzymes glutamate-cysteine ligase and glutathione synthetase, and the lysosomal protease cathepsin B, which can catabolize cysteine-rich extracellular proteins to produce additional cystine for fueling the synthesis of glutathione. Taken together, our results highlight the significant impact of cell size on cellular function and survival, revealing a size-dependent vulnerability to ferroptosis that could influence therapeutic strategies based on this cell death pathway.

INTRODUCTION

Cell size is fundamental to cell physiology. This is because it impacts cell geometry and sets the scale of all biosynthetic processes in the cell (Chan & Marshall, 2010; Ginzberg *et al*, 2015; Zatulovskiy & Skotheim, 2020). The importance of cell size is most clearly seen when yeast and mammalian cells become excessively large. In these cases, cells are not able to maintain optimal protein and mRNA concentrations to support growth as their cytoplasm becomes more dilute, unless the increase in cell size is coulter-balanced by the increase in cell ploidy (Neurohr *et al*, 2019; Lanz *et al*, 2022, 2024; Zatulovskiy *et al*, 2022). Such excessively large cells exhibit features of senescence and are no longer able to enter the cell division cycle. Unsurprisingly, cell size regulation is compromised in many diseases and during aging (Sandlin *et al*, 2022; Nguyen *et al*, 2016; Lengefeld *et al*, 2021). As animals, including humans, grow older, they contain more 'senescent' cells that tend to be larger (Davies *et al*, 2022). For example, basal keratinocytes are about 1.5 times as large when humans are 80 years old versus 20 (Liao *et al*, 2012). Conversely, cancer cells often exhibit an extreme heterogeneity in cell size, which may be associated with more proliferation (Sandlin *et al*, 2022; Nguyen *et al*, 2016; Li *et al*, 2015; Bell & Waizbard, 1986). Taken together, these studies argue for the importance of cell size in both natural and disease contexts.

Due to the importance of cell size for cell physiology, this property is highly regulated by distinct classes of molecular mechanisms. One class of mechanisms regulates the cell growth rate so that smaller cells grow faster and add proportionally more biomass than larger cells within one cell division cycle to ensure that all cells divide at similar sizes (Ginzberg *et al*, 2018; Liu *et al*, 2024; Conlon & Raff, 2003). A second class of molecular mechanisms, useful in more regular shaped cell types like rod shaped bacteria and fission yeast, relies on geometrical parameters such as cell length or surface area to measure cell size and determine that appropriate timing for initiating cell division (Miller *et al*, 2023; Martin & Berthelot-Grosjean, 2009; Pan *et al*, 2014; Bhatia *et al*, 2014; Moseley & Nurse, 2010). Finally, a third class of mechanisms rely on differential changes in protein concentrations of cell cycle activators and cell cycle inhibitors as cells grow larger (Chen *et al*, 2020b; Zatulovskiy *et al*, 2020; Schmoller *et al*, 2015). Typically, cell cycle activators either remain at constant concentration or increase with cell size, while some key cell cycle inhibitors, like the transcriptional inhibitors Whi5 in budding yeast and the retinoblastoma

protein RB in human cells, are progressively diluted in larger cells to trigger their division (Zatulovskiy *et al*, 2020; Schmoller *et al*, 2015; Zhang *et al*, 2022b, 2024).

That some larger cells initiate division through increases in the concentrations of cell cycle activators relative to cell cycle inhibitors was surprising because previous bulk studies showed that total protein concentration remained constant as cells grew larger. However, this constant concentration of total protein masked changes in the concentrations of individual proteins as cells grow larger, as revealed by a systematic quantitative proteomics analysis (Lanz *et al*, 2022, 2024; Zatulovskiy *et al*, 2022). The proteomics analyses revealed that as cell size increases, the concentrations of numerous senescence-related proteins begin to approach those of a senescent cell, even before cells lose the ability to enter the cell division cycle (Lanz *et al*, 2022; Crozier *et al*, 2023). This may in part explain the association of large cell size with the senescent state. Moreover, large cells have difficulty in replicating and repairing their genomes, which may be related to the lower concentrations of DNA replication and repair enzymes observed in larger cells (Lanz *et al*, 2022; Crozier *et al*, 2022; Manohar *et al*, 2023; Foy *et al*, 2023; Wilson *et al*, 2023). Taken together, these results indicate that a cell size increase in the absence of DNA replication impacts cell physiology through changing the composition of the proteome.

If cell size drives widespread changes in proteome composition, then this might impact many areas of cell physiology, including the susceptibility to cell death. Indeed, proteomic and transcriptomic comparisons of different-sized cells within the same cell type identified concentration changes for many genes involved in regulated cell death (Lanz *et al*, 2022; Miettinen & Björklund, 2016). Consistent with this, cell size is correlated with some cell death decisions – smaller cells have a higher likelihood to undergo apoptosis both in cell cultures and during *C. elegans* and *D. melanogaster* development (Miettinen & Björklund, 2016; Sethi *et al*, 2022; Kiyomitsu & Cheeseman, 2013; Hatzold & Conradt, 2008; Chen *et al*, 2016; Cordes *et al*, 2006). Inspired by these studies, we aimed to mechanistically investigate how cell size affects different cell death responses in human cells, as it remains unknown whether cell size impacts non-apoptotic cell death.

To test if there is a relationship between cell size and cell death, we used a high-throughput microscopy based approach to examine a variety of stresses (Forcina *et al*, 2017; Inde *et al*, 2020). We found that susceptibility to ferroptosis, an iron-dependent form of cell death, demonstrated the strongest dependence on cell size. This finding resonates with a recent report

100 that cell susceptibility to RSL3, a chemical that induces ferroptosis by inhibiting the reduction of
101 lipid peroxides by glutathione peroxidase 4 (GPX4), increases with cell size (Chan *et al*, 2025).
102 Inhibition of the cystine/glutamate antiporter system x_c^-, using the small molecule erastin2 (Era2)
103 (Dixon *et al*, 2014) preferentially induced cell death in smaller cells, while larger cells were more
104 resistant. Ferroptosis is characterized by the accumulation of toxic lipid peroxides (Jiang *et al*,
105 2021; Dixon & Olzmann, 2024). To suppress this accumulation and prevent ferroptosis, cells can
106 use cystine/cysteine-derived metabolites, like the reduced tripeptide glutathione (GSH), to
107 prevent the accumulation of peroxidized lipids. The lower susceptibility of large cells to Era2-
108 induced ferroptosis can likely be explained by our observation that larger cells are able to produce
109 higher amounts of GSH per unit protein mass, and that they have a lower concentration of
110 enzymes like ACSL4 that incorporate oxidizable polyunsaturated fatty acids into the plasma
111 membrane (Doll *et al*, 2017). Supporting this model, the genetic disruption of *ACSL4* reduced the
112 size dependence of lipid peroxidation and ferroptotic cell death. Taken together, our results show
113 how large cell size can protect against ferroptosis.
114

RESULTS

Larger cells are less susceptible to ferroptosis

To test our hypothesis that cell size affects susceptibility to cell death, we exposed cells of different sizes to a variety of compounds known to induce different forms of cell death. To do this, we first used fluorescence-activated cell sorting (FACS) to isolate small and large G1-phase HMEC-*hTERT* cells (human mammary epithelium cells immortalized with telomerase, herein referred to as HMEC for brevity) (Fig. 1A,B) (Lanz *et al*, 2022). We sorted cells for size using side scatter, which correlates well with cell size (Lanz *et al*, 2022; Tzur *et al*, 2011; Berenson *et al*, 2019). In this experiment we used DNA staining with Hoechst dye to only collect the cells that were in G1 phase of the cell cycle, since the cell cycle phase can influence cell survival (Rodencal *et al*, 2024; Ruiz-Losada *et al*, 2022; Lee *et al*, 2024; Kuganesan *et al*, 2023). The small- and large-sorted cells were then seeded into 384-well plates and treated with death-inducing compounds over a range of different doses. Each population of cells was then monitored using high-throughput fluorescence microscopy for 72 h to measure dose-dependent responses and cell death kinetics (Forcina *et al*, 2017; Inde *et al*, 2020).

Comparing dose-response curves for small and large cells across different compounds, we observed the largest size-dependent differences in cell death susceptibility in response to erastin2 (Era2). Era2 induces ferroptosis by inhibiting system x_c^- (Dixon *et al*, 2014). Larger HMEC cells were resistant to higher doses of Era2 than smaller cells. For example, at the 72 h time point, the Era2 IC_{50} was 28 ± 11 μM (mean ± SD) for large cells versus 2.0 ± 1.4 μM for small cells (Student's t-test: $p = 0.039$) (Fig. 1C). Moreover, larger cells exhibit slower cell death kinetics (Fig. 1D). By contrast, for compounds that cause cell death by disrupting protein synthesis (puromycin, anisomycin), inducing DNA damage (doxorubicin), inhibiting protein glycosylation (tunicamycin), or blocking proteasome function (bortezomib), IC_{50} values were not statistically significantly different for large versus small cells (Fig. 1E). We note that this does not eliminate the possibility that there are size-dependent differences in susceptibilities to these compounds that would manifest if our size range were expanded further. However, since the most pronounced differences were observed for Era2, we focused our investigation on how cell size affects ferroptosis.

148 To test if protection against ferroptosis by large cell size was generalizable beyond HMEC
149 cells isolated by FACS, we used alternative methods to generate different sized populations of
150 cells and tested additional cell lines. We examined the HT-1080 fibrosarcoma cell line, commonly
151 used in ferroptosis studies (Dixon *et al*, 2012), and non-transformed telomerase-immortalized
152 retinal pigment epithelium cells (RPE-1 cell line), commonly used in cell cycle and cell size
153 studies. We used FACS to sort G1-phase HT-1080 cells into four cell size bins and treated these
154 cells with 0.3 μM Era2. As observed in HMEC cells, larger HT-1080 and RPE-1 cells were more
155 resistant to ferroptotic cell death (Fig. S1A). Next, to generate populations of different-sized cells
156 without cell sorting, we arrested HT-1080 cells in early G1 using the cell-cycle inhibitor palbociclib
157 (CDK4/6 inhibitor) for 2-6 days (Neurohr *et al*, 2019; Lanz *et al*, 2022; Crozier *et al*, 2023; Manohar
158 *et al*, 2023; Foy *et al*, 2023). Larger cells, which were arrested in G1 for a longer time, were less
159 sensitive to Era2 than smaller cells arrested for a shorter duration (Fig. 2A,B). We note that non-
160 arrested cells had a lower susceptibility to Era2-induced ferroptosis compared to cells that were
161 arrested in G1 for 2-3 days, despite being smaller in size. This is likely due to the difference in the
162 fraction of cells in different cell cycle phases between arrested and non-arrested conditions since
163 cells in S/G2/M phases are known to be more resistant to ferroptosis than cells in G0/G1 phases
164 (Rodencal *et al*, 2024; Kuganesan *et al*, 2023).
165
166 We further confirmed that the effects of cell size on Era2-induced ferroptosis susceptibility
167 are generalizable across cell lines and independent of the cell cycle. To do this, we treated RPE1
168 cells with palbociclib for 2 or 4 days and then measured their susceptibility to Era2. Both the cells
169 treated with palbociclib for 2 days and for 4 days were arrested in G1, but the cells treated for 4
170 days were nearly two-fold larger than the cells treated for 2 days (Fig 2C,D). This enabled us to
171 isolate the effects of cell size from cell cycle effects and confirm that larger cells were significantly
172 more resistant to Era2-induced ferroptosis compared to their smaller counterparts in the same
173 phase of the cell cycle (Fig 2E).
174
175 As an additional means to generate populations of different sized cells, we used inducible
176 shRNA-mediated cyclin D1 (*CCND1*) knockdown in RPE-1 cells to generate a population of cells
177 that had larger cell sizes compared to uninduced RPE-1 cells (You *et al*, 2025). As previously
178 reported, cells that inducibly expressed *CCND1* shRNA had a ~30% decrease in Cyclin D1 protein
179 concentration but continued to grow and proliferate, though at a lower division rate (You *et al*,
180 2025). As a result, these *CCND1* knockdown cells were larger than uninduced cells, and were
181 less susceptible to Era2 (Fig. 2F,G).

182

183 Our finding that larger cells are less susceptible to ferroptosis induced by Era2 treatment
184 seemingly contradicted findings that large size sensitizes cells to the ferroptosis-inducing
185 compound RSL3 (Chan *et al*, 2025). Unlike Era2, which acts by inhibiting cystine/glutamate
186 antiporter system x_c^- and thereby depleting glutathione (GSH) pool, RSL3 belongs to a different
187 class of ferroptosis inducers, which acts by inhibiting glutathione peroxidase 4 (GPX4) (Yang *et*
188 *al*, 2014), a key enzyme that uses GSH to reduce toxic lipid peroxidation. To compare the effects
189 of these two classes of compounds in our experimental system, we treated the HT-1080 cells,
190 arrested in G1 for 2-6 days using palbociclib, with RSL3 (Fig. S1B). Consistent with the published
191 report (Chan *et al*, 2025) and in contrast to Era2 treatment (Fig. 2B), increased cell size during
192 G1 arrest progressively increased sensitivity to RSL3. This difference in cell responses to the two
193 different classes of ferroptosis inducers has been noted in several reports describing context-
194 dependent responses to different classes of ferroptosis inducers (Chan *et al*, 2025; Rodencal *et*
195 *al*, 2024; Magtanong *et al*, 2022).

196

197 Taken together, our measurements demonstrate that in human cell cultures, larger cells
198 are generally less susceptible to ferroptosis induced by system x_c^- inhibition (Fig. 2H). We
199 observed this result in populations of different sized cells that were generated through multiple
200 methods including genetics, FACS sorting, and small molecule-induced cell cycle arrest.

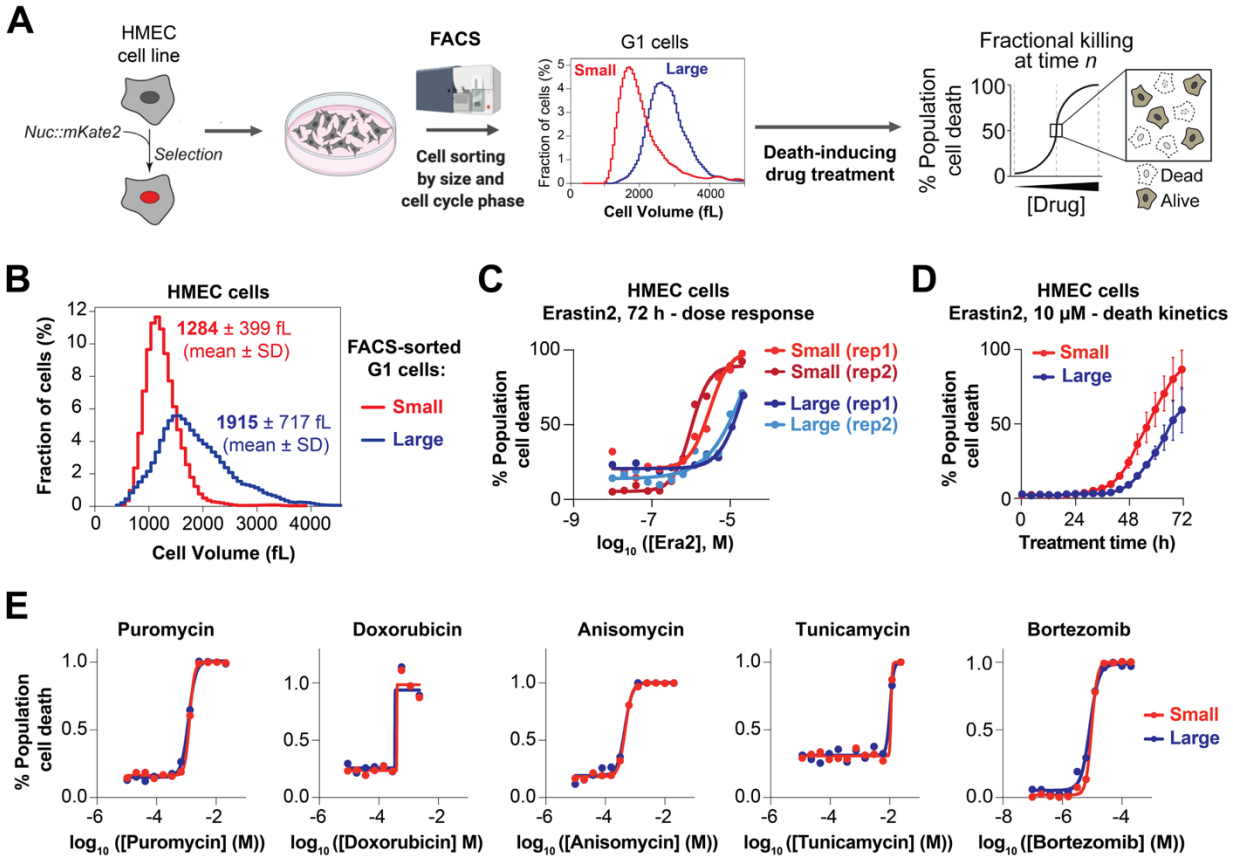

Figure 1. High-throughput microscopy-based measurement of cell death susceptibility in different-sized cells.

(A) Experiment schematic: a genetic construct encoding nuclear-localized fluorescent protein mKate2 was delivered into HMEC cells using lentiviral transduction. After selection, these cells were FACS-sorted by cell cycle phase and cell size into small and large G1 cells (smallest and largest 5%). The FACS-sorted cells were seeded on 384-well plates and allowed to settle overnight before being treated with death-inducing compounds in the media containing a dead-cell dye SYTOX Green. The cells were imaged for 72 h during treatment, and live cells were identified by the presence of nuclear mKate2 fluorescence, while dead cells were identified by the presence of the SYTOX Green signal (Forcina *et al*, 2017; Inde *et al*, 2020). The numbers of live and dead cells were automatically tracked over time to determine the dose-response curves and cell death kinetics.

(B) Cell size distributions of small and large G1-phase HMEC cells after FACS sorting, measured on a Coulter counter.

216 (C) Dose-response curves of small and large FACS-sorted HMEC cells treated with a
217 potent ferroptosis-inducing compound erastin2 (Era2). Rep1 and rep2 denote two different
218 biological replicates, each with two technical replicates.
219 (D) Cell death kinetics of small and large FACS-sorted HMEC cells treated with 10 μM
220 Era2. Dots show the means of two biological replicates, error bars denote the range.
221 (E) Dose-response curves of small and large FACS-sorted HMEC cells treated for 72 h
222 with other lethal compounds: puromycin, doxorubicin, anisomycin, tunicamycin and bortezomib.
223 Each experiment was performed twice independently, and each biological replicate included two
224 technical replicates. The dots show averages of two biological replicates.
225

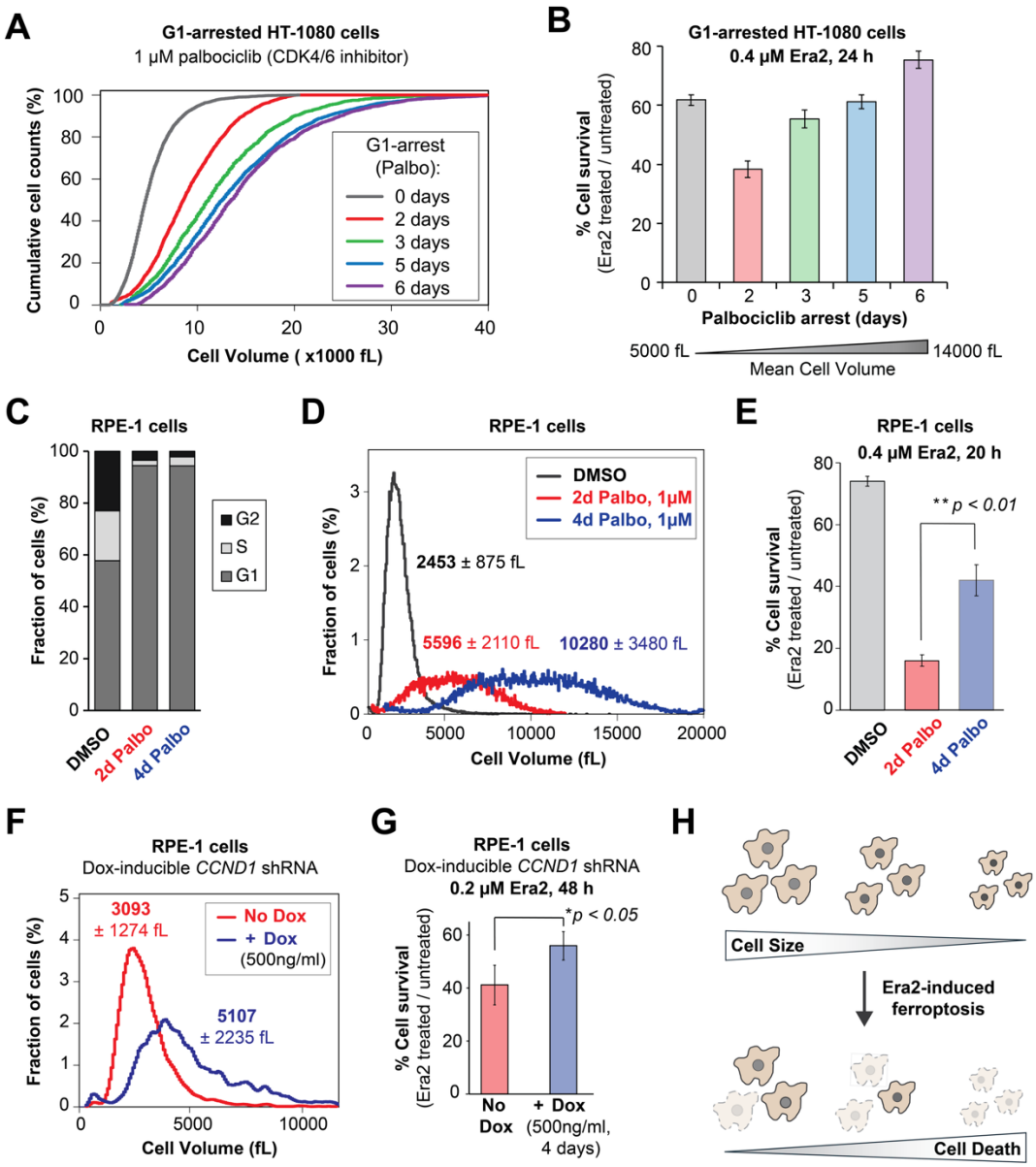

Figure 2. Larger cells are less susceptible to Era2-induced ferroptosis.

(A) Cumulative cell size distributions of HT-1080 cells, whose cell cycle was arrested in G1 phase for 0, 2, 3, 5, or 6 days with 1 μM of the CDK4/6 inhibitor palbociclib.

(B) Cell survival percentage of HT-1080 cells whose size was increased through palbociclib-induced cell cycle arrest. After pre-treatment with palbociclib for the indicated numbers of days, the cells were exposed to 0.4 μM Era2 in the presence of palbociclib for 24 h. Cell survival percentage was calculated relative to the cells treated only with palbociclib.

235 (C) Cell cycle phase distribution of asynchronously proliferating RPE-1 cells, and RPE-1
236 cells treated with the CDK4/6 inhibitor palbociclib for 2 or 4 days.
237 (D) Cell size distribution of asynchronously proliferating RPE-1 cells, and RPE-1 cells
238 treated with the CDK4/6 inhibitor palbociclib for 2 or 4 days. The numbers next to the histograms
239 indicate mean cell size ± standard deviation for the corresponding condition.
240 (E) Cell survival percentage in RPE-1 cells whose cell cycle was synchronized and size
241 was increased through 2-day or 4-day palbociclib-induced cell cycle arrest. After pre-treatment
242 with palbociclib for the indicated numbers of days, the cells were exposed to 0.4 μM Era2 in the
243 presence of palbociclib for 20 h. Cell survival percentage was calculated relative to the cells
244 treated only with palbociclib.
245 (F) Cell size distributions of RPE-1 cells that inducibly express shRNA against cyclin D1
246 gene (*CCND1*) to slow down the cell cycle and increase cell size. Cells were grown in medium
247 containing 500 ng/mL doxycycline for 4 days to induce shRNA expression and increase cell size.
248 Uninduced cells were grown in the same medium with DMSO in place of doxycycline.
249 (G) Cell survival percentage in control RPE-1 cells and cells expressing an shRNA against
250 cyclin D1 gene (*CCND1*). Cells were treated with 0.2 μM Era2 for 48 h, and cell survival
251 percentage was calculated relative to DMSO-treated cells. Cell survival percentages in graphs
252 (B), (E) and (G) are shown as means ± s.e.m.; n = 3 biological replicates. A two-tailed unpaired
253 Student's t-test was used to evaluate the statistical significance of survival percentage differences
254 in panels (E) and (G).
255 (H) Graphical summary: Larger cells are less susceptible to Era2-induced ferroptosis.
256
257

258

259 **Membrane lipid peroxidation decreases with cell size**

260

261 Ferroptosis is defined and caused by the accumulation of toxic products from
262 polyunsaturated fatty acid (PUFA) peroxidation in the plasma membrane (Jiang *et al*, 2021; Dixon
263 & Olzmann, 2024) (Fig. 3A). We therefore next sought to determine how cell size affects
264 ferroptosis-associated lipid peroxidation. Lipid peroxidation can be detected using a ratiometric
265 fluorescent sensor dye BODIPY-C11 581/591 (Dixon *et al*, 2012; Pap *et al*, 1999). This dye can
266 be used for ratiometric analysis of lipid peroxidation in flow cytometry, which detects a shift of the
267 fluorescence emission peak from red (~590 nm) to green (~510 nm) caused by the oxidation of
268 the polyunsaturated butadienyl portion of this fatty acid analog. When HMEC cells are treated
269 with Era2, which leads to increased lipid peroxidation, we find a decrease in non-oxidized (red)
270 BODIPY-C11 fluorescence and an increase in oxidized (green) BODIPY-C11 as expected (Fig.
271 3B).

272

273 To determine how cell size affects basal lipid peroxidation in cells, we first stained control
274 (DMSO-treated) cells with BODIPY-C11 and subjected them to a flow cytometry analysis using
275 side scatter (SSC-A) as a proxy for cell size (Lanz *et al*, 2022; Tzur *et al*, 2011). When we plotted
276 the oxidized to non-oxidized BODIPY-C11 ratio against cell size, we observed a clear anti-
277 correlation between these two parameters (Fig. 3C,D). We then performed a similar analysis on
278 Era2-treated cells. For this analysis, we gated only live cells using a fluorescent cell permeability
279 dye SYTOX Blue that stains dead or dying cells to omit cells undergoing Era2-induced death (Fig.
280 3E). This gating allowed us to exclusively focus on the live cells that were not dying. We found
281 that in Era2-treated cell populations, larger cells demonstrated lower levels of lipid peroxidation,
282 similarly to untreated cells (Fig. 3F). By contrast, membrane lipid peroxidation, the terminal cause
283 of ferroptosis, exhibits higher basal levels in smaller cells. This provided a rationale for why
284 smaller cells would require less treatment with Era2 to accumulate enough lipid peroxidation and
285 induce ferroptosis.

286

287 Having determined that membrane lipid peroxidation decreases with cell size, we next
288 investigated how the expression of key cellular components regulating this process changes with
289 cell size. The overall lipid oxidation status in the membrane is set largely by the competition
290 between Fe^{2+}-dependent peroxidation of PUFA-containing phospholipids, and glutathione-
291 dependent reduction of peroxidized lipids by GPX4 (Fig. 3A). We analyzed size-dependent

292 proteomics data for RPE-1 cells and primary human lung fibroblasts (HLF) and observed no
293 significant size-differences in GPX4 expression (Fig. 3G). However, ferritin heavy chain (FTH1)
294 and ferritin light chain (FTL) concentrations increased by 1.6-to-2-fold with a two-fold increase in
295 cell size (Fig. 3H,I). Ferritin acts as a key iron-storage protein that can promote ferroptosis
296 resistance through iron chelation (Zhang *et al*, 2022a; Chen *et al*, 2020a). The observed increase
297 in ferritin concentration with cell size could therefore lead to additional Fe^{2+} ion chelation, which
298 in turn would protect large cells from iron-dependent lipid peroxidation and ferroptosis. However,
299 when we measured the concentration of labile intracellular Fe^{2+} using a fluorescent probe
300 FerroOrange (Hirayama *et al*, 2020), we did not observe any size-dependent decrease in labile
301 iron concentration (Fig. S2A). Previous work suggests a link between increased sequestration of
302 ferrous iron in lysosomes and resistance to ferroptosis. It was reported that senescent cells, which
303 are also large (Fig. S3A,B), gain resistance to ferroptosis through lysosomal alkalinization and
304 sequestration of ferrous iron in lysosomes (Loo *et al*, 2025). We therefore tested whether the
305 superscaling of lysosomes observed in large cells (Lanz *et al*, 2022; You *et al*, 2025) promotes
306 Era2 resistance through lysosomal iron sequestration. To do this, we stained the cells with the
307 lysosomal iron detection probe Lyso-FerroRed (Saimoto *et al*, 2025) and measured its scaling
308 using flow cytometry (Fig. S2B). We observed that the amount of Lyso-FerroRed, and therefore,
309 the amount of lysosomal iron, scaled in direct proportion to cell size, just like the total cellular
310 protein content (Fig. S2B). These results indicate that iron chelation by ferritin and its
311 sequestration in lysosomes are unlikely to play a crucial role in size-dependent decrease in Era2
312 sensitivity.
313

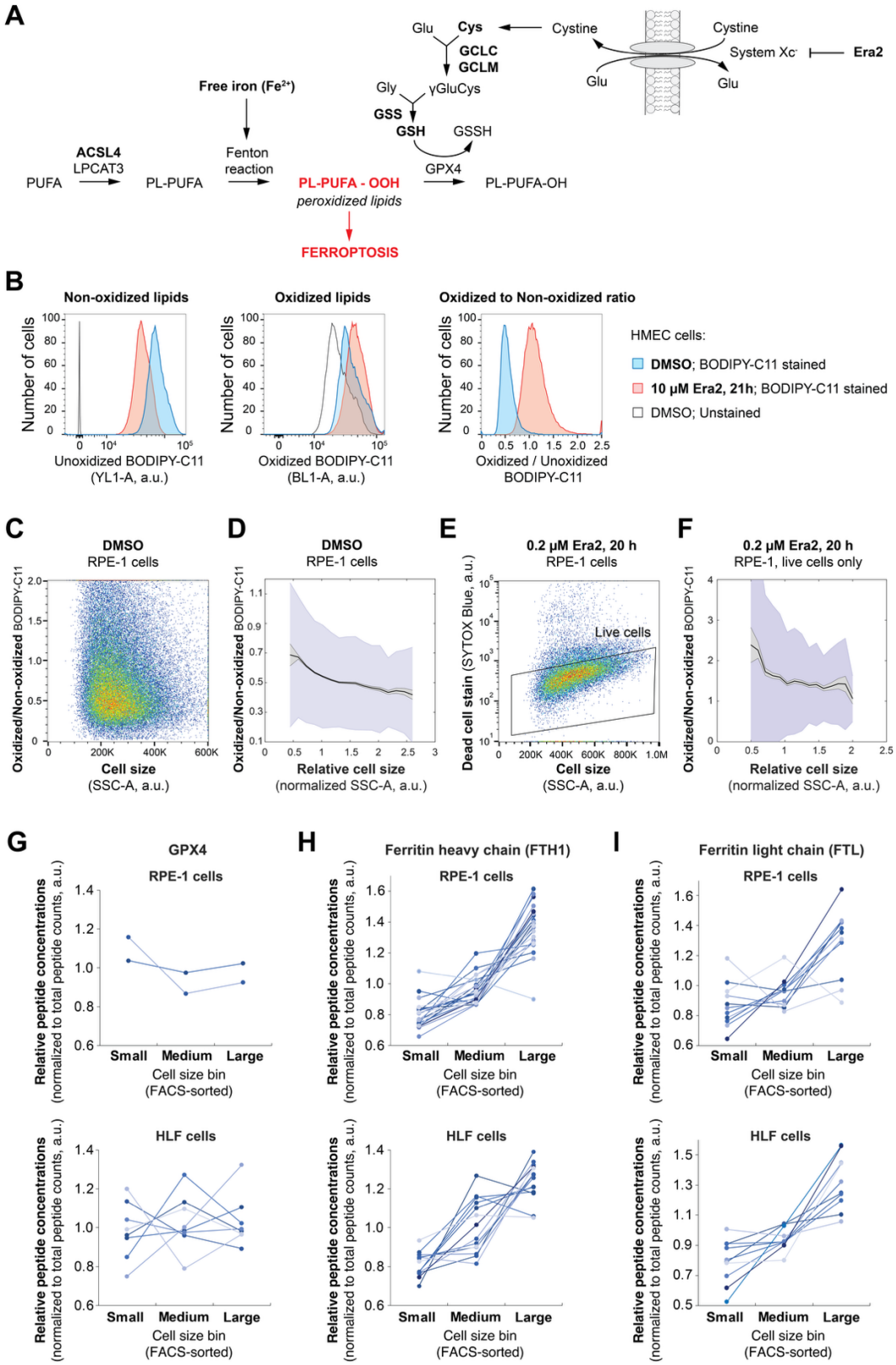

Figure 3. Membrane lipid peroxidation decreases with cell size.

317 (A) Schematic of pathways regulating ferroptosis. Ferroptosis is induced through the
318 accumulation of toxic peroxidized lipid species in the plasma membrane. The accumulation of
319 peroxidized lipids is prevented by glutathione (GSH) production and GSH-dependent reduction of
320 the peroxidized lipids (Jiang *et al*, 2021; Dixon & Olzmann, 2024).
321 (B) The ratiometric fluorescent dye BODIPY-C11 581/591 detects lipid peroxidation in live
322 HMEC cells (Dixon *et al*, 2012; Pap *et al*, 1999). Oxidation of the polyunsaturated butadienyl
323 portion of this fatty acid analog results in a shift of the fluorescence emission peak from red (~590
324 nm) to green (~510 nm), allowing ratiometric analysis of lipid peroxidation using flow cytometry.
325 Treatment of cells with Era2 increases lipid peroxidation, as indicated by decreased non-oxidized
326 (red) BODIPY-C11 fluorescence and increased oxidized (green) BODIPY-C11 fluorescence.
327 (C) A flow cytometry analysis of lipid peroxidation in different-sized RPE-1 cells within the
328 DMSO-treated cell culture. The side-scatter parameter (SSC-A) was used as a proxy for cell size
329 (Lanz *et al*, 2022; Tzur *et al*, 2011). Three biological replicates were performed, and 100,000
330 events were recorded for each.
331 (D) A quantitative analysis of the flow cytometry data from panel (C): the data were binned
332 into 12 bins by normalized cell size (SSC-A / median SSC-A), and the mean values for of oxidized
333 (green) to non-oxidized (red) BODIPY-C11 ratio were plotted for each bin (black line). Gray
334 shaded area denotes the s.e.m. for each bin, and the blue area denotes the standard deviation.
335 (E) For Era2-treated cell populations, live cells were identified and gated in the indicated
336 region using a live/dead cell permeability dye SYTOX Blue.
337 (F) Size-dependent lipid peroxidation in RPE-1 cells treated with 0.2 μM Era2 for 20 h.
338 The analysis was performed as in panel (D).
339 (G-I) Proteomics-based analysis of GPX4 (G), ferritin heavy chain (H) and ferritin light
340 chain (I) expression in FACS-sorted small, medium and large RPE-1 cells and primary lung
341 fibroblasts (HLF). Each line in the plot corresponds to a unique peptide from the indicated proteins
342 identified by mass spectrometry reported in *Lanz et al.* (Lanz *et al*, 2022).
343

344

345 **Larger cells have higher concentrations of glutathione**

346

347 Having shown that lipid peroxidation decreases with cell size and that such a decrease is
348 unlikely to be mediated by changes in labile Fe^{2+} concentration, we next sought to test if cell size
349 also affects glutathione (GSH) abundance, which contributes to oxidized lipid reduction and
350 ferroptosis resistance, and is depleted in cells upon system x_c^- inhibition (but not GPX4 inhibition)
351 (Jiang *et al*, 2021; Dixon & Olzmann, 2024; Dixon *et al*, 2012) (Fig. 3A). To determine how cell
352 size affects glutathione synthesis, we re-analyzed our previously collected proteomics data,
353 where we compared the proteomes of FACS-sorted small, medium, and large RPE-1 cells (Lanz
354 *et al*, 2022) (Fig. 3). We found that concentrations of two key proteins involved in GSH
355 biosynthesis, glutamate-cysteine ligase modifier subunit (GCLM) and glutathione synthetase
356 (GSS), increase with cell size. This indicates that larger cells might have higher GSH production
357 rates (Fig. 4A).

358

359 While the upregulation of GSH biosynthesis may promote the resistance of larger cells to
360 ferroptosis, such an upregulation alone cannot explain why larger cells become more resistant to
361 ferroptosis induced by the cystine import inhibitor Era2, but not, for example, by the GPX4 inhibitor
362 RSL3 (Chan *et al*, 2025) (Figs. 2B, S1B). We found previously that upon mTORC1 inhibition cells
363 can evade cystine deprivation-induced ferroptosis by uptake and catabolism of cysteine-rich
364 extracellular proteins, mostly albumin (Armenta *et al*, 2022) (Fig. S3C). This process involves
365 albumin degradation in lysosomes, predominantly by cathepsin B (CatB), and subsequent export
366 of cystine from lysosomes to fuel the synthesis of glutathione. Large cells undergo proteome
367 rearrangements similar to those occurring upon mTORC1 inhibition (Zatulovskiy *et al*, 2022). This
368 suggests that large cells may upregulate CatB expression to bypass the Era2-induced cystine
369 import inhibition via system x_c^-. To test this hypothesis, we used flow cytometry to measure how
370 the expression of cathepsin B and the system x_c^- cystine/glutamate transporter SLC7A11 (xCT)
371 scales with cell size (Fig. 4B). We found that SLC7A11 concentration modestly decreases, while
372 CatB concentration significantly increases with cell size (Fig. 4B). This shift in the ratio between
373 SLC7A11 and CatB supports the hypothesis that larger cells may rely less on cystine import via
374 system x_c^- and thus become more resistant to system x_c^- inhibition by Era2.

375

376 To further test the prediction that larger cells have more GSH to protect against ferroptosis,
377 we measured GSH abundance in different-sized cells using flow cytometry. To do this, we stained

378 the cells with the fluorescent GSH probe monochlorobimane (MCB) (Rice *et al*, 1986; Shrieve *et*
379 *al*, 1988). In addition to MCB, we also stained the same cells with the total protein dye CFSE
380 (carboxyfluorescein diacetate succinimidyl ester) (Lanz *et al*, 2022; Berenson *et al*, 2019), which
381 allowed us to calculate relative cell size-dependent changes in glutathione concentrations
382 (amounts of glutathione per unit protein mass; Fig. 4C-H). While total protein amounts scaled in
383 proportion to cell size (Fig. 4G), the amount of MCB-reactive GSH 'super-scaled' so that larger
384 cells have higher glutathione concentrations than smaller cells (Fig. 4F,H-J). Overall, these
385 findings indicate that larger cells have higher concentrations of glutathione, likely due to their
386 higher concentrations of GSH producing enzymes and cathepsin B, which could specifically
387 protect them from system x_c^- inhibition-induced ferroptosis.
388

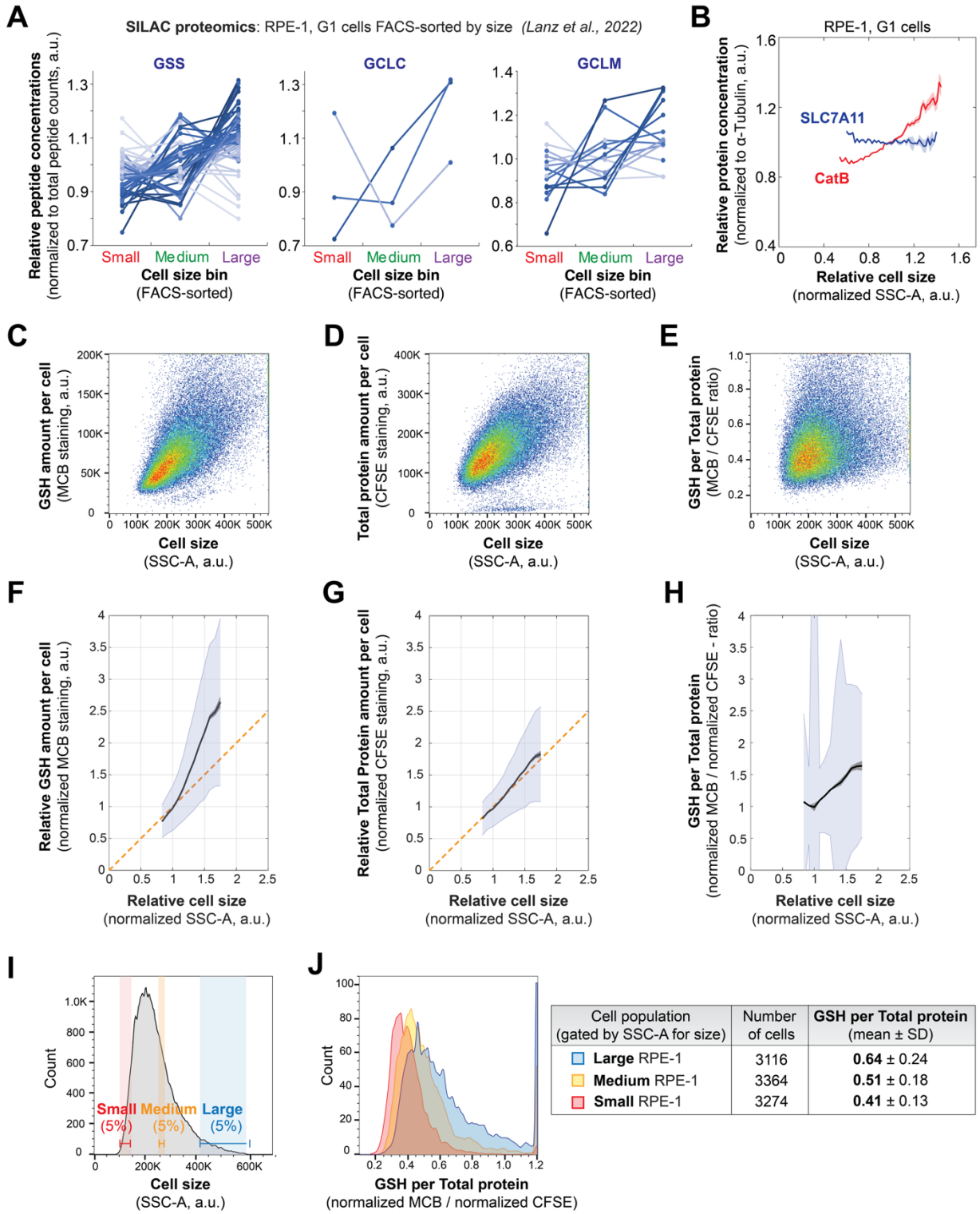

Cell population (gated by SSC-A for size)	Number of cells	GSH per Total protein (mean ± SD)
Large RPE-1	3116	**0.64** ± 0.24
Medium RPE-1	3364	**0.51** ± 0.18
Small RPE-1	3274	**0.41** ± 0.13

Figure 4. Larger cells have higher concentrations of glutathione and enzymes promoting glutathione synthesis.

393 (A) Proteomics-based analysis indicates the concentrations of key enzymes involved in
394 glutathione production (see Fig. 3A) increase with cell size. For this analysis, RPE-1 cells were
395 FACS-sorted into populations of small, medium, and large G1 cells, and the proteomes of cells in
396 these bins were analyzed using SILAC mass spectrometry. The primary proteomics data used to
397 plot the concentrations of glutathione synthetase (GSS), glutamate-cysteine ligase catalytic
398 (GCLC) and modifier (GCLM) subunits were taken from our previous work (Lanz *et al*, 2022).
399 Each line in the plot corresponds to a unique peptide corresponding to the indicated protein that
400 was identified by mass spectrometry.
401 (B) Flow-cytometry-based measurement of cystine/glutamate transporter SLC7A11 (xCT)
402 and cathepsin B (CatB) concentrations in G1-phase RPE-1 cells demonstrates a modest
403 decrease in SLC7A11 and a significant increase in cathepsin B concentrations with cell size. To
404 calculate the concentrations of SLC7A11 and CatB, their amounts were measured with flow
405 cytometry using immunofluorescence and normalized to the amounts of α-Tubulin. The data were
406 binned by cell size, and mean values for each bin were plotted against normalized cell size (solid
407 blue line for SLC7A11 and red line for CatB). Shaded areas denote the s.e.m. for each bin.
408 (C, D) Flow-cytometry-based measurement of GSH amount (C) and total protein amount
409 (D) scaling with cell size in RPE-1 cells. The side scatter parameter (SSC-A) is used as a proxy
410 for cell size (Tzur *et al*, 2011; Berenson *et al*, 2019). Three biological replicates were performed,
411 and 100,000 events were recorded in each replicate.
412 (E) GSH concentration in RPE-1 cells plotted against cell size. The GSH concentration is
413 calculated as the ratio of GSH amount to the amount of total protein from data shown in panels
414 (C) and (D).
415 (F-H) Analysis of the flow cytometry data shown in panels (C-E). The data were binned by
416 cell size, and mean values (black lines in the plots) for GSH amount (F), total protein amount (G)
417 and GSH concentration (H) were plotted against normalized cell size (SSC-A / median SSC-A).
418 Gray shaded areas denote the s.e.m. for each bin, and the blue area denotes the standard
419 deviation. The orange line in (F) and (G) is shown for reference and corresponds to a perfect
420 scaling scenario, where the amount of a cell component increases in direct proportion to cell size
421 so that its concentration does not change. The total amount of protein is very close to perfect
422 scaling, while the amount of GSH increases faster than cell size so that its concentration is higher
423 in larger cells.
424 (I, J) Comparison of GSH concentrations in small, medium, and large cells. Based on the
425 flow cytometry data, 5% smallest, 5% largest and 5% intermediate-sized RPE-1 cells were gated
426 (I), and their GSH concentration (GSH amount per total protein amount) histograms were plotted

427 for each of these size populations (J). The plot shows that the GSH concentration distributions
428 progressively shift towards higher values when cell size increases. The plots in (I-J) are based on
429 the primary data shown in panels (C-D).
430

431

432 **Higher concentrations of ACSL4 in smaller cells drives increased membrane lipid**
433 **peroxidation**

434

435 Besides the increase in GSH-producing enzyme concentrations with cell size, our
436 proteomics data also indicate that the concentration of another key protein involved in ferroptosis,
437 Acyl-CoA Synthetase Long Chain Family Member 4 (ACSL4), also changed significantly with cell
438 size (Fig. 4A). ACSL4 promotes ferroptosis sensitivity by enriching phospholipid and
439 triacylglycerol pools with ω-6 PUFAs that are prone to peroxidation (Doll *et al*, 2017) (Fig. 3A).
440 Our proteomics data (Lanz *et al*, 2022) suggested that ACSL4 concentration decreases with cell
441 size (Fig. 5A). To confirm this finding using flow cytometry, we stained the cells with antibodies
442 against ACSL4. We observed that the ACSL4 concentration indeed decreases with cell size, while
443 the concentration of the control protein β-actin remains constant (Fig. 5B). This suggested the
444 lower lipid peroxidation in larger calls may be due in part to lower ACSL4 abundance.

445

446 To test the role of ACSL4 in size-dependent lipid peroxidation, we measured lipid
447 peroxidation in wild-type and *ACSL4* gene-disrupted HT-1080 cells (Magtanong *et al*, 2019). We
448 stained the cells with BODIPY-C11 and measured fluorescence with flow cytometry. While lipid
449 peroxidation decreased with increasing cell size in wild-type HT-1080 cells, we did not observe
450 any such size-dependence in *ACSL4 KO* cells (Magtanong *et al*, 2019) (Fig. 5C,D). This indicated
451 that ACSL4 activity was required for size-dependent changes in basal lipid peroxidation, which
452 likely makes smaller cells more susceptible to ferroptosis.

453

454 To test the hypothesis that size-dependent expression of ACSL4 mediates the increased
455 resistance of larger cells to ferroptosis, we FACS-sorted *ACSL4 KO* HMEC cells into small,
456 medium and large size bins and assessed their responses to Era2 (Figs. 5E,F and S4). In this
457 experiment, we synchronized cells in G1 phase using palbociclib prior to cell sorting and also
458 incubated the sorted cells in the presence of palbociclib during Era2 treatment to isolate cell size
459 effects from the previously observed confounding effects of the cell cycle on ferroptosis (Fig.
460 2B,E). Consistent with our hypothesis, genetic disruption of *ACSL4* reduced the size dependence
461 of the ferroptotic response in Era2-treated HMEC cells (Fig. 5F). We note that while genetic
462 disruption of *ACSL4* significantly reduced the size dependence of ferroptosis, it does not eliminate
463 the size-dependence completely. This might be because ferroptosis is driven by two parallel

464 processes – ACSL4-dependent PUFA incorporation into the membrane and subsequent lipid
465 peroxidation (Fig. 3), both of which depend on cell size.
466

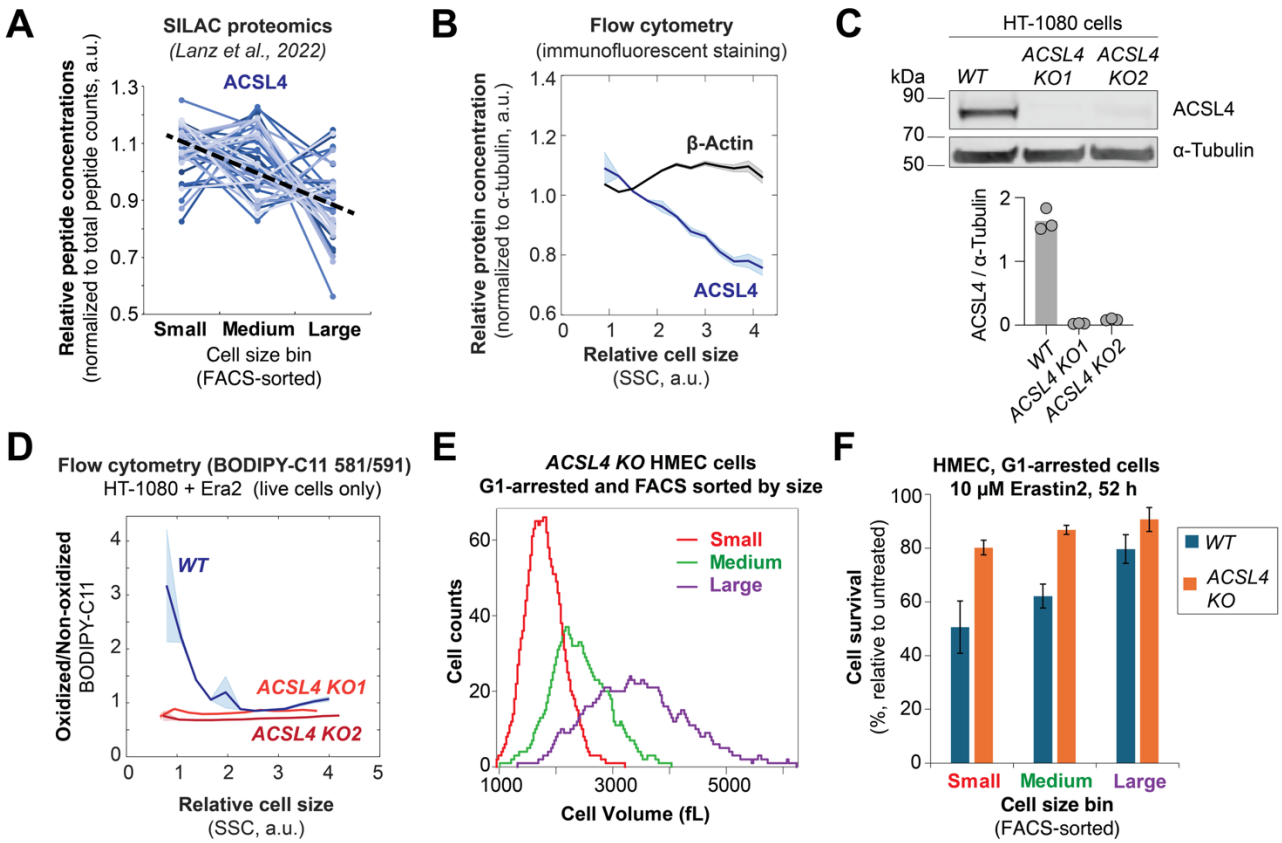

Figure 5. Higher expression of ACSL4 in smaller cells drives increased lipid peroxidation and ferroptosis.

(A) Proteomics analysis identified the size-dependent expression of ACSL4, an enzyme that enriches cellular membranes with long polyunsaturated fatty acids prone to peroxidation (Doll *et al*, 2017). The primary proteomics data were from our previous work (Lanz *et al*, 2022). Each line in the plot corresponds to a unique peptide from the ACSL4 protein identified by mass spectrometry; the dashed black line indicated the average ACSL4 protein slope.

(B) Flow cytometry analysis confirms the decrease of ACSL4 concentration with cell size in HMEC cells. β-Actin was measured as a reference protein, as its concentration does not change with cell size. To calculate the concentrations of ACSL4 and β-Actin, their amounts were measured with flow cytometry using immunofluorescence and were normalized to the amounts of α-Tubulin. The data were binned by cell size, and mean values for each bin were plotted against normalized cell size (solid blue line for ACSL4 and black line for β-Actin). Shaded areas denote the s.e.m. for each bin.

(C) Validation of *ACSL4* knockout in HT-1080 cells with immunoblotting. Wild-type (*WT*) HT-1080 cell line and two different *ACSL4* knockout clones (*KO1* and *KO2*) were analyzed using

485 antibodies against ACSL4 and α-Tubulin as a loading control. Bar plot shows the quantification
486 of immunoblotting data from three biological replicates.
487 (D) Deletion of *ACSL4* eliminates the size-dependence of membrane lipid peroxidation in
488 HT-1080 cells. The plot shows the flow cytometry measurements of lipid peroxidation after 16 h
489 1 μM Era2 treatment in wild-type and *ACSL4 KO* HT-1080 cells (*ACSL4 KO1* and *ACSL4 KO2*
490 are two different knock-out clones) (Magtanong *et al*, 2019). The ratio between oxidized (green)
491 BODIPY-C11 and non-oxidized (red) BODIPY-C11 fluorescence is plotted as a metric for lipid
492 peroxidation, and the side-scatter parameter (SSC-A) is used as a proxy for cell size. The flow
493 cytometry data were binned by cell size, and mean values of oxidized to non-oxidized BODIPY-
494 C11 ratios were plotted for each bin (blue solid line corresponds to *wild-type* cells, orange and
495 red lines correspond to *ACSL4* gene-disrupted clones *KO1* and *KO2*). Shaded areas denote the
496 s.e.m. for each bin.
497 (E) Cell size distributions of small, medium, and large G1-arrested *ASCL4 KO* HMEC cells
498 isolated by FACS sorting. Prior to FACS sorting, the cells were cultured for 24 h in the presence
499 of 1 μM palbociclib to synchronize cells in G1 phase. Cell size after sorting was measured on a
500 Coulter counter.
501 (F) Cell survival percentage in *WT* and *ACSL4 KO* HMEC cells, sorted into small, medium,
502 and large size bins by FACS. After sorting, the cells were re-plated in the presence of 1 μM
503 palbociclib to keep them in G1 phase. Cells were then treated with 10 μM Era2 for 52 h, and the
504 cell survival percentage was calculated relative to palbociclib-only treated cells. Cell survival
505 percentages in graphs are shown as means ± s.e.m. for n = 3 biological replicates.
506

507

508 **DISCUSSION**

509

510 In this study, we found that larger cells are less susceptible to ferroptotic cell death induced
511 by the system x_c^- inhibitor erastin2 (Fig. 6). This observation may explain previous findings where
512 genetic alterations that reduce cell size also promote ferroptosis, whereas those that increase cell
513 size inhibit it. For instance, deletion of p21, which decreases cell size, sensitizes to ferroptosis,
514 whereas overexpression of p21, increasing cell size, confers ferroptosis resistance (Tarangelo *et*
515 *al*, 2018; Venkatesh *et al*, 2020). Similarly, deletion of the retinoblastoma protein (RB), which also
516 reduces cell size, promotes ferroptosis. Moreover, further deletion of additional RB family
517 members, p107 and p130, in a triple knockout that drastically reduces cell size, increases
518 sensitivity to ferroptosis (Kuganesan *et al*, 2021; Sage *et al*, 2000). Here, we demonstrate that
519 isogenic cell populations differing only in size exhibit different susceptibilities to ferroptosis. This
520 implies that many genetic interactions associated with ferroptosis may actually operate indirectly
521 through their effects on cell size.

522

523

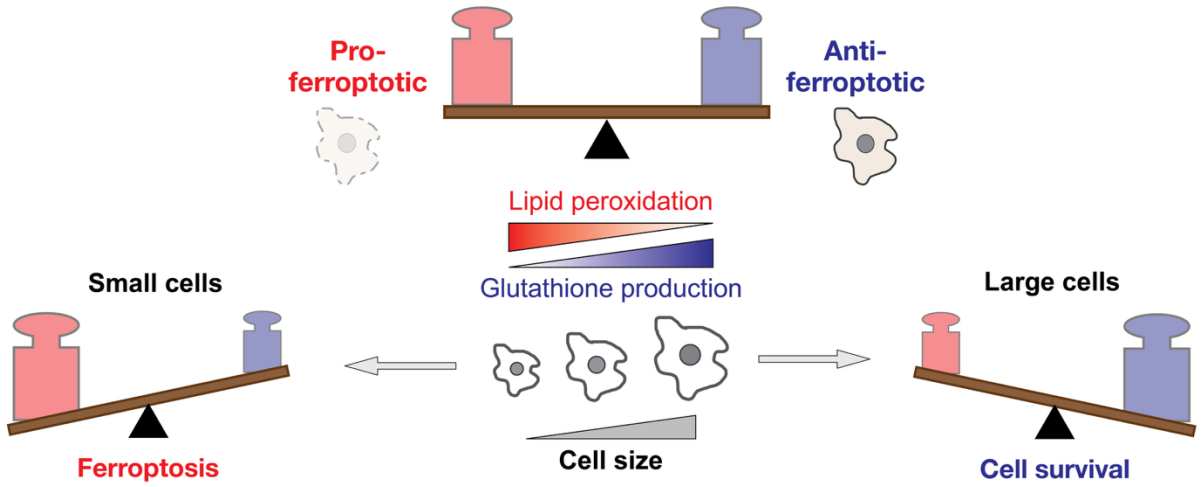

524

525

526 **Figure 6. Cell size modulates cell susceptibility to ferroptosis.** Larger cells are less
527 prone to Era2-induced cell death because they generate less peroxidized plasma membrane
528 lipids and more glutathione to reduce those toxic peroxidized lipids.

529

530

That increased cell size protects against system x_c^- inhibitor-induced ferroptosis has important implications for how this form of cell death interacts with the cell division cycle. Cells in G1 phase of the cell cycle were reported to be more susceptible to ferroptosis (Rodencal *et al*, 2024; Kuganesan *et al*, 2023), which suggested that ferroptosis inducers could be used in combination with cancer drugs, like the CDK4/6 inhibitor palbociclib, that arrest cells in G1 phase of the cell cycle (Herrera-Abreu *et al*, 2024). However, while CDK4/6 inhibitors arrest cells in G1, they do not inhibit cell growth, such that the longer they are arrested, the larger the cells grow (Lanz *et al*, 2022; Crozier *et al*, 2023; Manohar *et al*, 2023). This results in a complex, non-monotonic ferroptotic response dynamics in cells treated with CDK4/6 inhibitors (Fig. 2B,E). Just following CDK4/6 inhibitor treatment, as more and more cells are arrested in G1 phase, cells become more sensitive to both RSL3- and erastin-induced ferroptosis (Kuganesan *et al*, 2023; Rodencal *et al*, 2024). However, the longer the cells are arrested, the larger they become, which further promotes their susceptibility to RSL3 (Fig. S1B) but reduces their susceptibility to Era2-induced ferroptosis (Fig. 2B). The fact that the cell cycle arrest and cell size increase have opposing effects on Era2-induced ferroptosis susceptibility could explain why different studies reported seemingly contradictory results, where sometimes an increased and sometimes a decreased or unchanged sensitivity to system x_c^- inhibitors was observed depending on the cell type, duration and type of cell cycle arrest (Lee *et al*, 2024; Kuganesan *et al*, 2023; Rodencal *et al*, 2024). Such complex interplay between the cell cycle and cell size effects on ferroptosis suggests that combination therapies utilizing CDK4/6 inhibitors and ferroptosis inducers would have to carefully choose a dosage schedule. Additionally, our data suggest that previously reported resistance of senescent cells to ferroptosis can at least partially be due to the increased cell size, a well-established hallmark of senescence (Davies *et al*, 2022).

That small cells are more prone to ferroptosis is likely related to their proteome and metabolome composition differing from that of larger cells. Here, we found that larger cells both generate fewer peroxidized membrane lipids and accumulate more glutathione, which can be used to reduce and thus detoxify the peroxidized lipids (Fig. 6). Likely, these size-dependent changes in lipid oxidation and glutathione abundance are due to differential cell-size-scaling of different metabolic enzymes in the cell. Larger cells also have higher concentrations of iron-chelating protein ferritin and glutathione-producing enzymes GSS and GCLM that protect cells against ferroptosis, and have lower concentrations of the enzyme ACSL4, which promotes ferroptosis. Indeed, the genetic disruption of *ACSL4* greatly reduced the size-dependence of

565 membrane lipid peroxidation, a ferroptosis trigger, and makes ferroptosis less size-dependent.
566 Taken together, these observations indicate that the size-dependent remodeling of the proteome
567 underlies much of the size-dependent sensitivity to ferroptosis.
568
569 The fact that larger cell size promotes increased ferroptosis resistance to system x_c^-
570 inhibitors (Era2) but, at the same time, decreased resistance to ferroptosis induced by GPX4
571 inhibitors (RSL3) suggests that the critical roles in these two types of responses are played by
572 different molecular pathways. This finding supports the notion that the ferroptotic cell death
573 response is highly context-dependent and varies dramatically depending on the cell type and
574 class of stimuli inducing ferroptosis (Rodencal *et al*, 2024; Magtanong *et al*, 2022; Soula *et al*,
575 2020). While a decreased cell sensitivity to Era2 in larger cells is due to size-dependent increase
576 in glutathione production and decrease in unsaturated lipid incorporation into the membrane by
577 ACSL4, the increased sensitivity to RSL3 is reported to be mediated mainly by ER expansion,
578 iron accumulation, and lipid accumulation and remodeling (Chan *et al*, 2025). We show that large
579 cells may become resistant specifically to Era2 but not RSL3 through the upregulation of
580 lysosomal function, particularly cathepsin B expression, which enables the uptake and catabolism
581 of cysteine-rich extracellular proteins. A size-dependent shift in the ratio between SLC7A11 and
582 cathepsin B makes large cells less dependent on cystine import via system x_c^-, and thus, more
583 resistant to Era2. In addition to this, it was reported that RSL3 can induce ferroptosis
584 independently of GPX4 and may target other selenoproteins (DeAngelo *et al*, 2025; Cheff *et al*,
585 2023), which could also contribute to the difference in size-dependent responses to RSL3 and
586 Era2.
587
588 In conclusion, our finding that the response of cells to ferroptosis inducers is influenced
589 by cell size point to a broader pattern where cellular decisions are often size-dependent. A general
590 size-dependence of cellular decisions may be driven by widespread changes in protein and
591 metabolite composition taking place as cells grow larger. Indeed, larger cells differ markedly from
592 their smaller counterparts, which likely affects key decisions related to cell death, division, and
593 differentiation. Previous studies, including our own, have explored how cell size influences cell
594 division and contributes to cellular senescence (Lanz *et al*, 2022; Zatulovskiy *et al*, 2022; Crozier
595 *et al*, 2023, 2022; Manohar *et al*, 2023; Foy *et al*, 2023; Wilson *et al*, 2023; Demidenko &
596 Blagosklonny, 2008). Here, we have demonstrated that cell size also plays a significant role in
597 modulating susceptibility specifically to ferroptotic cell death. Furthermore, research in
598 developmental biology shows that cell size can dictate developmental outcomes, as seen in the

599 asymmetrical division of neurosecretory motor neuron neuroblasts in *C. elegans* and cell fate
600 determination in *Arabidopsis* leaves (Sethi *et al*, 2022; Gong *et al*, 2023). Thus, we anticipate
601 many cellular decisions will be impacted by cell size, the fundamental mode of cell geometry that
602 sets the basic scale of all intracellular processes.
603

ACKNOWLEDGEMENTS

We thank Leslie Magtanong for assistance with the initial cell death screen design and all members of the Zatulovskiy and Skotheim laboratories for valuable discussions and feedback on this project. Cell sorting for this project was performed on an instrument in the Stanford Shared FACS Facility purchased by Parker Institute for Cancer Immunotherapy, and an instrument in the University of Cambridge, Department of Pathology FACS facility. We thank both FACS facilities for their assistance. This work was supported by a Chan Zuckerberg Biohub Investigator Award (J.M.S.), the NIH (P01 CA254867 grant to J.M.S. and R01 GM122923 to S.J.D.), and the Medical Research Council (MR/X020290/1 Career Development Award to E.Z.).

AUTHOR CONTRIBUTIONS

E.Z. conceived this study. E.Z., M.B.M., S.J.D., and J.M.S. designed the experiments. E.Z., M.B.M., and S.Z. performed the experiments and analyzed the experimental data. E.Z. and J.M.S. wrote the manuscript. E.Z., M.B.M., S.J.D., and J.M.S. edited the manuscript.

623
624 **MATERIALS AND METHODS**
625
626 **Cell culture conditions and cell lines**
627
628 Non-transformed *hTERT*-immortalized human mammary epithelium cells (HMEC-*hTERT*
629 cells, in this paper referred to simply as HMEC for brevity) were obtained from Stephen Elledge's
630 laboratory at Harvard Medical School (Solimini *et al*, 2012) and cultured in MEGM™ Mammary
631 Epithelial Cell Growth Medium (Lonza CC-3150). HT-1080 cells were purchased from ATCC
632 (Manassas, Virginia, USA). Non-transformed *hTERT*-immortalized human retinal pigment
633 epithelium cells (cell line RPE-1) were obtained from the Stearns laboratory at Stanford. Both the
634 HT-1080 and RPE-1 cell lines were grown in Dulbecco's modification of Eagle's medium (DMEM)
635 with L-glutamine, 4.5 g/L glucose and sodium pyruvate (Corning), supplemented with 10% FBS
636 (Corning) and 1% penicillin/streptomycin. All cells were cultured at 37ºC with 5% CO_2. HT-1080
637 cell lines expressing nuclear-localized fluorescent protein mKate2 (Nuc::mKate2) were generated
638 by lentiviral transduction of a viral vector at an M.O.I. of 0.3, that directed the expression of
639 nuclear-localized mKate2 (Forcina *et al*, 2017). Polyclonal mKate2-expressing populations were
640 selected using puromycin (1.5 mg/mL, 72 h). *ACSL4 KO* HT-1080 and HMEC cells were
641 generated using a CRISPR/Cas9 system, as described previously (Magtanong *et al*, 2019). RPE-
642 1 cells carrying a genetic construct for a conditional knock-down of cyclin D1 gene (*CCND1)*
643 through doxycycline-inducible *CCND1* shRNA expression were obtained from the Ioannis
644 Sanidas laboratory at Harvard Medical School.
645

646 **Immunofluorescence cell staining for flow cytometry**
647
648 For flow cytometry analysis, cells were grown on dishes to ~50% confluence and
649 harvested by trypsinization. The cells were then fixed with 3% formaldehyde for 10 min at 37ºC
650 and permeabilized with 90% methanol for 30 min on ice. Fixed and permeabilized cells were
651 washed once with PBS, blocked with 3% BSA in PBS for 30 min at 37ºC, and then stained with
652 primary antibodies for 2 h at 37ºC (rat-anti-alpha-Tubulin (Abcam, #ab6160), mouse-anti-Actin
653 (Sigma-Aldrich, #A2103), rabbit-anti-ACSL4 (Proteintech, #22401-1-AP), rabbit-anti-Cathepsin B
654 (Proteintech, #12216-1-AP), rabbit-anti-xCT/SLC7A11 (Cell Signaling Technology, #12691T)).
655 The cells were then washed twice with a wash buffer (1% BSA in PBS + 0.05% Tween® 20),

656 stained with the fluorophore-conjugated secondary antibodies Alexa Fluor 488 goat anti-rat (Life
657 Technologies, #A11006), Alexa Fluor 594 goat anti-rabbit (Life Technologies, #A11037), and
658 Alexa Fluor 647 goat anti-mouse (Thermo Fisher Scientific, #A32728) at 1:1000 dilution for 1 h at
659 37ºC. The cells were then washed again twice. After this treatment, the cells were resuspended
660 in PBS containing 3 μM DAPI for DNA staining, incubated for 10 min at room temperature, and
661 then analyzed on an Attune NxT flow cytometer (Thermo Fisher Scientific). Around 100.000 cells
662 were typically recorded for each sample, and three biological replicates were performed for each
663 experiment. The flow cytometry gating strategy is shown in Fig. S5. Briefly, single cells were gated
664 based on FSC-A vs SSC-A, then FSC-A vs FSC-H, then SSC-A vs SSC-W plots. From this
665 population of single cells, G1 cells were selected using Hoechst-A vs FSC-A plot (Fig. S5).
666 For plotting, all protein amounts and cell size values were normalized to the means for
667 each sample. To compensate for the nonspecific background staining of cells with antibodies, we
668 measured the fluorescence of cells stained with nonspecific Isotype Control antibodies. We then
669 performed a linear regression of this nonspecific background signal with cell size and subtracted
670 the background fluorescence corresponding to each cell's size from the actual anti-ACSL4
671 fluorescence signal measured for each cell. For all binned flow cytometry data plots, the cells
672 below the 2nd and above the 98th cell size percentiles were excluded to remove the extreme
673 outliers. Then, the remaining data were binned by size and plotted as background-corrected
674 average fluorescence intensity for each bin against the bin's average cell size. Bins with fewer
675 than 200 cells were excluded from the analysis to reduce noise. For protein concentration
676 calculation, the amount of the indicated protein in the cell was normalized to the amount
677 housekeeping protein alpha-Tubulin, which scales in proportion to cell volume (Lanz *et al*, 2022).
678

679 **Lipid peroxidation measurement with BODIPY-C11 581/591 fluorescent dye**

680

681 For lipid peroxidation analysis, cells were treated with DMSO or erastin2 (Era2) for 24 h
682 before being harvested by trypsinization. A cell suspension containing ~200,000 cells was then
683 transferred to a 1.5 mL microfuge tube. Cells were then pelleted by centrifugation (400 x g, 5 min)
684 and resuspended in BODIPY-C11 581/591 (5 μM) dissolved in HBSS. A dead cell stain SYTOX
685 Blue (Molecular Probes, #S34857) was added to cell suspensions at a final concentration of 20
686 nM to identify and exclude from the analysis all non-intact (dead or dying) cells. Cell suspensions
687 were incubated at 37°C for 20 min and then pelleted (400 x *g*, 5 min) and resuspended in 0.2 mL
688 of PBS buffer. Samples were strained through a cell strainer prior to flow cytometry analysis. Flow

689 cytometry analysis was performed on an Attune NxT flow cytometer (Thermo Fisher Scientific).
690 Oxidation of BODIPY-C11 581/591 was calculated as the ratio of the green fluorescence (BL1
691 channel, indicates oxidized probe) to the red fluorescence (YL1 channel, indicates unoxidized
692 probe) (Dixon *et al*, 2012; Pap *et al*, 1999).
693

694 **Single-cell glutathione (GSH) measurements with MCB fluorescent dye**

695

696 To measure the GSH amounts in different-sized cells using flow cytometry, we stained the
697 cells with the fluorescent GSH probe monochlorobimane (MCB) (Rice *et al*, 1986; Shrieve *et al*,
698 1988). To do this, the cells were harvested by trypsinization, resuspended in PBS at a density of
699 one million cells per mL, and incubated with 40 μM MCB (Invitrogen, #M1381MP). At the same
700 time, we stained with MCB, we also stained the same cells with a total protein dye CFSE
701 (CarboxyFluorescein Succinimidyl Ester). For total protein staining, the CellTrace CFSE dye
702 (Molecular Probes, #C34554) was added to cell suspensions at a 5 μM concentration. The cells
703 were then stained with MCB and CFSE for 20 min in a tissue culture incubator (37°C, 5% CO_2) in
704 the dark. The reactions were terminated using 1 mL cold complete medium, followed by
705 centrifugation (400 x *g*, 5 min, +4°C). The pelleted cells were then re-suspended in 0.2 mL of
706 PBS, filtered through a 40 μm cell strainer into FACS tubes and placed on ice. The MCB and
707 CFSE fluorescence signals were measured with an Attune NxT flow cytometer (Thermo Fisher
708 Scientific). GSH concentrations (amounts of glutathione per unit protein mass) in individual cells
709 were calculated as a ratio between the MCB signal (glutathione amount) and CFSE signal (total
710 protein amount).
711

712 **Intracellular iron detection with fluorescent probes**

713

714 To measure labile intracellular iron (Fe^{2+}) concentration, live RPE-1 cells were stained
715 simultaneously with three fluorescent probes - FerroOrange (Dojindo Laboratories, Japan, #
716 F374-10) to measure the amounts of labile Fe^{2+} in the cell, CellTrace CFSE dye (Molecular
717 Probes, #C34554) to measure total cellular protein amount, and Hoechst 33342 DNA stain
718 (Thermo Scientific, #62249) to determine the cell cycle phase of the cells. Prior to staining, the
719 cells on a dish were washed twice with warm (37ºC) serum-free DMEM and harvested by
720 trypsinization, followed by centrifugation and supernatant removal. The cell pellets were then
721 resuspended in a staining solution containing 1 μM FerroOrange, 5 μM CFSE and 20 μM Hoechst

722 in warm serum-free DMEM and incubated at 37°C for 30 min in a 5% CO2 incubator. After the
723 staining the cells were kept on ice and measured on an Attune NxT flow cytometer (Thermo Fisher
724 Scientific). Hoechst signal was used to select G1-phase cells for subsequent analysis.
725 A similar protocol was used to measure lysosomal Fe^{2+} amounts, but instead of
726 FerroOrange the cells were stained with 1 μM Lyso-FerroRed probe (Dojindo Laboratories, Japan,
727 # L270-10). After Lyso-FerroRed staining, the cells were centrifuged and washed twice with
728 serum-free DMEM prior to the flow cytometry measurement.
729

730 **Fluorescence-activated cell sorting (FACS)**

731

732 Fluorescence-activated cell sorting was used to sort live cells by their size and cell cycle
733 phase, as described previously (Lanz *et al*, 2022). Cells were harvested from dishes by
734 trypsinization, stained with 20 μM Hoechst 33342 DNA dye in PBS for 15 min at 37ºC, and then
735 sorted on a BD FACSAria Fusion flow cytometer. Consecutive SSC-A over FSC-A, and FSC-H
736 over FSC-A gates were used to isolate single cells. Then, G1 cells were gated by DNA content
737 (Hoechst staining). Finally, we collected the 10% smallest and 10% largest cells using the gating
738 based on SSC-A signal as a proxy for cell size. During sorting, all cell samples and collection
739 tubes were kept at 4ºC. To determine the cell size distributions of the collected samples, aliquots
740 were taken from each sorted size bin and measured on a Z2 Coulter counter (Beckman). Sorted
741 cells were re-plated for subsequent evaluation of their sensitivity to cell-death-inducing chemicals.
742

743 **Microscopy-based analysis of cell death kinetics**

744

745 For the analysis of cell death susceptibility, FACS-sorted small and large G1-phase cells
746 were seeded on a 384-well plate (100-1500 cells per well), allowed to adhere overnight, and then
747 treated with cell-death-inducing compounds for 72 h. Besides these lethal compounds, the cell
748 culture media also contained 20 nM of the dead-cell dye SYTOX Green (Molecular Probes,
749 #S7020), which permeates dying cells and produces a strong green fluorescent signal in cell
750 nuclei. Cells were imaged on the Essen IncuCyte Zoom and analyzed using scalable time-lapse
751 analysis of cell death kinetics (STACK) as described below. Two or three independent biological
752 replicates were performed for each experimental condition. Each of the biological replicates
753 contained two technical replicates for each condition that were then averaged for cell-death
754 sensitivity quantification. Cell death responses were measured using the scalable time-lapse

755 analysis of cell death kinetics (STACK) technique (Forcina *et al*, 2017; Inde *et al*, 2020). Cell lines
756 stably expressing nuclear-localized mKate2 were incubated in medium with 20 nM SYTOX Green
757 and the indicated cell-death-inducing compounds. Counts of live (mKate2+) and dead (SG+)
758 objects were obtained from images acquired every 4 h on the Essen IncuCyte Zoom (Essen
759 BioScience, Ann Arbor, MI). The following image extraction parameter values were used for
760 automated image analysis. For SG+ objects (dead cells): Adaptive Threshold Adjustment 3; Edge
761 Split On; Edge Sensitivity −7; Filter Area min 0 μm^2, max 750 μm^2. For mKate2+ objects (live
762 cells): Adaptive Threshold Adjustment 2.5; Edge Split On; Edge Sensitivity −2; Filter Area min 50
763 μm^2, maximum 8100 μm^2; Eccentricity max 0.9. For Overlap objects: Filter area min 50 μm^2,
764 maximum 8100 μm^2. Counts were exported to MS Excel (Microsoft Corporation, Redmond, WA)
765 and lethal fraction (LF) scores were computed from mKate2+ and SG+ counts, with the additional
766 step of removing 'overlap' double positive counts from live cell counts at each timepoint, as
767 described before (Forcina *et al*, 2017; Inde *et al*, 2020). LF scores were exported to Prism 9.0.1
768 (GraphPad Software, La Jolla, CA) for curve fitting and data plotting.
769

770 **Immunoblotting**

771 For immunoblotting, cells were lysed in RIPA lysis buffer on ice. Proteins from lysates
772 were separated on 10% SDS-PAGE gels and transferred to nitrocellulose membranes.
773 Membranes were then blocked with SuperBlock™ (TBS) Blocking Buffer (Thermo Fisher
774 Scientific) and incubated overnight at 4°C with primary antibodies in 3% BSA solution in PBS.
775 The primary antibodies used were: anti-ACSL4 (Sigma-Aldrich , #SAB2701949; 1:2500 dilution)
776 and anti-tubulin (Millipore Sigma, #MS581P1; 1:2000 dilution). The primary antibodies were
777 detected using the fluorescently labeled secondary antibodies IRDye® 680LT Goat anti-Mouse
778 IgG (LI-COR 926-68020) and IRDye® 800CW Goat anti-Rabbit IgG (LI-COR 926-32211).
779 Membranes were imaged on a LI-COR Odyssey CLx and analyzed with LI-COR Image Studio
780 software.

781

782 **Data quantification, statistical analysis, and software**

783

784 Lethal fraction calculations and statistical analyses of cell death were performed using
785 Microsoft Excel 14.6.0 (Microsoft Corporation, USA). Flow cytometry data were analyzed using

FlowJo 10.6.1 (FlowJo LLC, USA) and Matlab R2022b (MathWorks, USA). Graphing was performed using Prism 9 (GraphPad Software, La Jolla, CA).

REFERENCES

Armenta DA, Laqtom NN, Alchemy G, Dong W, Morrow D, Poltorack CD, Nathanson DA, Abu-Remaileh M & Dixon SJ (2022) Ferroptosis inhibition by lysosome-dependent catabolism of extracellular protein. *Cell Chemical Biology* 29: 1588-1600.e7

Bell CD & Waizbard E (1986) Variability of cell size in primary and metastatic human breast carcinoma. *Invasion Metastasis* 6: 11–20

Berenson DF, Zatulovskiy E, Xie S & Skotheim JM (2019) Constitutive expression of a fluorescent protein reports the size of live human cells. *Mol Biol Cell* 30: 2985–2995

Bhatia P, Hachet O, Hersch M, Rincon S, Berthelot-Grosjean M, Dalessi S, Basterra L, Bergmann S, Paoletti A & Martin SG (2014) Distinct levels in Pom1 gradients limit Cdr2 activity and localization to time and position division. *Cell Cycle* 13: 538–552

Chan KY, Yu Y, Kong Y, Cheng L, Yao R, Yin Chair PS, Wang P, Wang R, Sun W-Y, He R-R, *et al* (2025) GPX4-dependent ferroptosis sensitivity is a fitness trade-off for cell enlargement. *iScience* 28: 112363

Chan Y-HM & Marshall WF (2010) Scaling properties of cell and organelle size. *Organogenesis* 6: 88–96

Cheff DM, Huang C, Scholzen KC, Gencheva R, Ronzetti MH, Cheng Q, Hall MD & Arnér ESJ (2023) The ferroptosis inducing compounds RSL3 and ML162 are not direct inhibitors of GPX4 but of TXNRD1. *Redox Biol* 62: 102703

Chen C, Inaba M, Venkei ZG & Yamashita YM (2016) Klp10A, a stem cell centrosome-enriched kinesin, balances asymmetries in Drosophila male germline stem cell division. *eLife* 5: e20977

Chen X, Yu C, Kang R & Tang D (2020a) Iron Metabolism in Ferroptosis. *Front Cell Dev Biol* 8

Chen Y, Zhao G, Zahumensky J, Honey S & Futcher B (2020b) Differential Scaling of Gene Expression with Cell Size May Explain Size Control in Budding Yeast. *Molecular Cell* 78: 359-370.e6

Conlon I & Raff M (2003) Differences in the way a mammalian cell and yeast cells coordinate cell growth and cell-cycle progression. *J Biol* 2: 7

Cordes S, Frank CA & Garriga G (2006) The C. elegans MELK ortholog PIG-1 regulates cell size asymmetry and daughter cell fate in asymmetric neuroblast divisions. *Development* 133: 2747–2756

822 Crozier L, Foy R, Adib R, Kar A, Holt JA, Pareri AU, Valverde JM, Rivera R, Weston WA, Wilson
823 R, *et al* (2023) CDK4/6 inhibitor-mediated cell overgrowth triggers osmotic and
824 replication stress to promote senescence. *Mol Cell* 83: 4062-4077.e5

825 Crozier L, Foy R, Mouery BL, Whitaker RH, Corno A, Spanos C, Ly T, Gowen Cook J & Saurin
826 AT (2022) CDK4/6 inhibitors induce replication stress to cause long-term cell cycle
827 withdrawal. *EMBO J* 41: e108599

828 Davies DM, van den Handel K, Bharadwaj S & Lengefeld J (2022) Cellular enlargement - A
829 new hallmark of aging? *Frontiers in Cell and Developmental Biology* 10

830 DeAngelo SL, Zhao L, Dziechciarz S, Shin M, Solanki S, Balia A, El-Derany MO, Castillo C,
831 Qin Y, Das NK, *et al* (2025) Recharacterization of the Tumor Suppressive Mechanism
832 of RSL3 Identifies the Selenoproteome as a Druggable Pathway in Colorectal
833 Cancer. *Cancer Res* 85: 2788–2804

834 Demidenko ZN & Blagosklonny MV (2008) Growth stimulation leads to cellular senescence
835 when the cell cycle is blocked. *Cell Cycle* 7: 3355–3361

836 Dixon SJ, Lemberg KM, Lamprecht MR, Skouta R, Zaitsev EM, Gleason CE, Patel DN, Bauer
837 AJ, Cantley AM, Yang WS, *et al* (2012) Ferroptosis: An Iron-Dependent Form of
838 Nonapoptotic Cell Death. *Cell* 149: 1060–1072

839 Dixon SJ & Olzmann JA (2024) The cell biology of ferroptosis. *Nat Rev Mol Cell Biol*: 1–19

840 Dixon SJ, Patel DN, Welsch M, Skouta R, Lee ED, Hayano M, Thomas AG, Gleason CE,
841 Tatonetti NP, Slusher BS, *et al* (2014) Pharmacological inhibition of cystine–
842 glutamate exchange induces endoplasmic reticulum stress and ferroptosis. *eLife* 3:
843 e02523

844 Doll S, Proneth B, Tyurina YY, Panzilius E, Kobayashi S, Ingold I, Irmler M, Beckers J, Aichler
845 M, Walch A, *et al* (2017) ACSL4 dictates ferroptosis sensitivity by shaping cellular
846 lipid composition. *Nat Chem Biol* 13: 91–98

847 Forcina GC, Conlon M, Wells A, Cao JY & Dixon SJ (2017) Systematic Quantification of
848 Population Cell Death Kinetics in Mammalian Cells. *cels* 4: 600-610.e6

849 Foy R, Crozier L, Pareri AU, Valverde JM, Park BH, Ly T & Saurin AT (2023) Oncogenic signals
850 prime cancer cells for toxic cell overgrowth during a G1 cell cycle arrest. *Molecular*
851 *Cell* 83: 4047-4061.e6

852 Ginzberg MB, Chang N, D'Souza H, Patel N, Kafri R & Kirschner MW (2018) Cell size sensing
853 in animal cells coordinates anabolic growth rates and cell cycle progression to
854 maintain cell size uniformity. *Elife* 7: e26957

855 Ginzberg MB, Kafri R & Kirschner M (2015) Cell biology. On being the right (cell) size.
856 *Science* 348: 1245075

857 Gong Y, Dale R, Fung HF, Amador GO, Smit ME & Bergmann DC (2023) A cell size threshold
858 triggers commitment to stomatal fate in Arabidopsis. *Science Advances* 9: eadf3497

859 Hatzold J & Conradt B (2008) Control of Apoptosis by Asymmetric Cell Division. *PLOS*
860 *Biology* 6: e84

861 Herrera-Abreu MT, Guan J, Khalid U, Ning J, Costa MR, Chan J, Li Q, Fortin J-P, Wong WR,
862 Perampalam P, *et al* (2024) Inhibition of GPX4 enhances CDK4/6 inhibitor and
863 endocrine therapy activity in breast cancer. *Nat Commun* 15: 9550

864 Hirayama T, Niwa M, Hirosawa S & Nagasawa H (2020) High-Throughput Screening for the
865 Discovery of Iron Homeostasis Modulators Using an Extremely Sensitive
866 Fluorescent Probe. *ACS Sens* 5: 2950–2958

867 Inde Z, Forcina GC, Denton K & Dixon SJ (2020) Kinetic Heterogeneity of Cancer Cell
868 Fractional Killing. *Cell Reports* 32: 107845

869 Jiang X, Stockwell BR & Conrad M (2021) Ferroptosis: mechanisms, biology and role in
870 disease. *Nat Rev Mol Cell Biol* 22: 266–282

871 Kiyomitsu T & Cheeseman IM (2013) Cortical Dynein and Asymmetric Membrane
872 Elongation Coordinately Position the Spindle in Anaphase. *Cell* 154: 391–402

873 Kuganesan N, Dlamini S, Tillekeratne LMV & Taylor WR (2021) Tumor suppressor p53
874 promotes ferroptosis in oxidative stress conditions independent of modulation of
875 ferroptosis by p21, CDKs, RB, and E2F. *J Biol Chem* 297: 101365

876 Kuganesan N, Dlamini S, Tillekeratne VL & Taylor WR (2023) Regulation of Ferroptosis by
877 Transcription Factor E2F1 and RB. doi:10.21203/rs.3.rs-2493335/v1 [PREPRINT]

878 Lanz MC, Zatulovskiy E, Swaffer MP, Zhang L, Ilerten I, Zhang S, You DS, Marinov G,
879 McAlpine P, Elias JE, *et al* (2022) Increasing cell size remodels the proteome and
880 promotes senescence. *Molecular Cell* 82: 3255-3269.e8

881 Lanz MC, Zhang S, Swaffer MP, Ziv I, Götz LH, Kim J, McCarthy F, Jarosz DF, Elias JE &
882 Skotheim JM (2024) Genome dilution by cell growth drives starvation-like proteome
883 remodeling in mammalian and yeast cells. *Nat Struct Mol Biol* 31: 1859–1871

884 Lee H, Horbath A, Kondiparthi L, Meena JK, Lei G, Dasgupta S, Liu X, Zhuang L, Koppula P, Li
885 M, *et al* (2024) Cell cycle arrest induces lipid droplet formation and confers
886 ferroptosis resistance. *Nat Commun* 15: 79

887 Lengefeld J, Cheng C-W, Maretich P, Blair M, Hagen H, McReynolds MR, Sullivan E, Majors
888 K, Roberts C, Kang JH, *et al* (2021) Cell size is a determinant of stem cell potential
889 during aging. *Sci Adv* 7: eabk0271

890 Li Q, Rycaj K, Chen X & Tang DG (2015) Cancer stem cells and cell size: A causal link?
891 *Semin Cancer Biol* 35: 191–199

892 Liao Y-H, Chen S-Y, Chou S-Y, Wang P-H, Tsai M-R & Sun C-K (2012) Determination of
893 chronological aging parameters in epidermal keratinocytes by in vivo harmonic
894 generation microscopy. *Biomed Opt Express* 4: 77–88

895 Liu X, Yan J & Kirschner MW (2024) Cell size homeostasis is tightly controlled throughout
896 the cell cycle. *PLOS Biology* 22: e3002453

897 Loo TM, Zhou X, Tanaka Y, Sugawara S, Yamauchi S, Kawasaki H, Matsuoka Y, Sugiura Y,
898 Sakuma S, Yamanishi Y, *et al* (2025) Senescence-associated lysosomal dysfunction
899 impairs cystine deprivation-induced lipid peroxidation and ferroptosis. *Nat*
900 *Commun* 16: 6617

901 Magtanong L, Ko P-J, To M, Cao JY, Forcina GC, Tarangelo A, Ward CC, Cho KY, Patti GJ,
902 Nomura DK, *et al* (2019) Exogenous Monounsaturated Fatty Acids Promote a
903 Ferroptosis-Resistant Cell State. *Cell Chem Biol* 26: 420-432.e9

904 Magtanong L, Mueller GD, Williams KJ, Billmann M, Chan K, Armenta DA, Moffat J, Boone C,
905 Myers CL, Olzmann JA, *et al* (2022) Context-Dependent Regulation of Ferroptosis
906 Sensitivity. *Cell Chem Biol*: S2451-9456(22)00236–7

907 Manohar S, Estrada ME, Uliana F, Vuina K, Alvarez PM, de Bruin RAM & Neurohr GE (2023)
908 Genome homeostasis defects drive enlarged cells into senescence. *Mol Cell* 83:
909 4032-4046.e6

910 Martin SG & Berthelot-Grosjean M (2009) Polar gradients of the DYRK-family kinase Pom1
911 couple cell length with the cell cycle. *Nature* 459: 852–856

912 Miettinen TP & Björklund M (2016) Cellular Allometry of Mitochondrial Functionality
913 Establishes the Optimal Cell Size. *Dev Cell* 39: 370–382

914 Miller KE, Vargas-Garcia C, Singh A & Moseley JB (2023) The fission yeast cell size control
915 system integrates pathways measuring cell surface area, volume, and time. *Current*
916 *Biology* 33: 3312-3324.e7

917 Moseley JB & Nurse P (2010) Cell Division Intersects with Cell Geometry. *Cell* 142: 189–193

918 Neurohr GE, Terry RL, Lengefeld J, Bonney M, Brittingham GP, Moretto F, Miettinen TP, Vaites
919 LP, Soares LM, Paulo JA, *et al* (2019) Excessive Cell Growth Causes Cytoplasm
920 Dilution And Contributes to Senescence. *Cell* 176: 1083-1097.e18

921 Nguyen A, Yoshida M, Goodarzi H & Tavazoie SF (2016) Highly variable cancer
922 subpopulations that exhibit enhanced transcriptome variability and metastatic
923 fitness. *Nat Commun* 7: 11246

924 Pan KZ, Saunders TE, Flor-Parra I, Howard M & Chang F (2014) Cortical regulation of cell
925 size by a sizer cdr2p. *eLife* 3: e02040

926 Pap EH, Drummen GP, Winter VJ, Kooij TW, Rijken P, Wirtz KW, Op den Kamp JA, Hage WJ &
927 Post JA (1999) Ratio-fluorescence microscopy of lipid oxidation in living cells using
928 C11-BODIPY(581/591). *FEBS Lett* 453: 278–282

929 Rice GC, Bump EA, Shrieve DC, Lee WL & Kovacs MK (1986) Quantitative Analysis of
930 Cellular Glutathione by Flow Cytometry Utilizing Monochlorobimane: Some
931 Applications to Radiation and Drug Resistance in Vitro and in Vivo. *Cancer Research*
932 46: 6105–6110

933 Rodencal J, Kim N, He A, Li VL, Lange M, He J, Tarangelo A, Schafer ZT, Olzmann JA, Long JZ,
934 *et al* (2024) Sensitization of cancer cells to ferroptosis coincident with cell cycle
935 arrest. *Cell Chem Biol* 31: 234-248.e13

936 Ruiz-Losada M, González R, Peropadre A, Gil-Gálvez A, Tena JJ, Baonza A & Estella C (2022)
937 Coordination between cell proliferation and apoptosis after DNA damage in
938 Drosophila. *Cell Death Differ* 29: 832–845

939 Sage J, Mulligan GJ, Attardi LD, Miller A, Chen S, Williams B, Theodorou E & Jacks T (2000)
940 Targeted disruption of the three Rb-related genes leads to loss of G1 control and
941 immortalization. *Genes Dev* 14: 3037–3050

942 Saimoto Y, Kusakabe D, Morimoto K, Matsuoka Y, Kozakura E, Kato N, Tsunematsu K,
943 Umeno T, Kiyotani T, Matsumoto S, *et al* (2025) Lysosomal lipid peroxidation
944 contributes to ferroptosis induction via lysosomal membrane permeabilization. *Nat*
945 *Commun* 16: 3554

946 Sandlin CW, Gu S, Xu J, Deshpande C, Feldman MD & Good MC (2022) Epithelial cell size
947 dysregulation in human lung adenocarcinoma. *PLOS ONE* 17: e0274091

948 Schmoller KM, Turner JJ, Kõivomägi M & Skotheim JM (2015) Dilution of the cell cycle
949 inhibitor Whi5 controls budding-yeast cell size. *Nature* 526: 268–272

950 Sethi A, Wei H, Mishra N, Segos I, Lambie EJ, Zanin E & Conradt B (2022) A caspase–
951 RhoGEF axis contributes to the cell size threshold for apoptotic death in developing
952 Caenorhabditis elegans. *PLOS Biology* 20: e3001786

953 Shrieve DC, Bump EA & Rice GC (1988) Heterogeneity of cellular glutathione among cells
954 derived from a murine fibrosarcoma or a human renal cell carcinoma detected by
955 flow cytometric analysis. *Journal of Biological Chemistry* 263: 14107–14114

956 Solimini NL, Xu Q, Mermel CH, Liang AC, Schlabach MR, Luo J, Burrows AE, Anselmo AN,
957 Bredemeyer AL, Li MZ, *et al* (2012) Recurrent Hemizygous Deletions in Cancers May
958 Optimize Proliferative Potential. *Science* 337: 104–109

959 Soula M, Weber RA, Zilka O, Alwaseem H, La K, Yen F, Molina H, Garcia-Bermudez J, Pratt
960 DA & Birsoy K (2020) Metabolic determinants of cancer cell sensitivity to canonical
961 ferroptosis inducers. *Nat Chem Biol* 16: 1351–1360

962 Tarangelo A, Magtanong L, Bieging-Rolett KT, Li Y, Ye J, Attardi LD & Dixon SJ (2018) p53
963 Suppresses Metabolic Stress-Induced Ferroptosis in Cancer Cells. *Cell Rep* 22:
964 569–575

965 Tzur A, Moore JK, Jorgensen P, Shapiro HM & Kirschner MW (2011) Optimizing Optical Flow
966 Cytometry for Cell Volume-Based Sorting and Analysis. *PLOS ONE* 6: e16053

967 Venkatesh D, Stockwell BR & Prives C (2020) p21 can be a barrier to ferroptosis
968 independent of p53. *Aging (Albany NY)* 12: 17800–17814

969 Wilson GA, Vuina K, Sava G, Huard C, Meneguello L, Coulombe-Huntington J, Bertomeu T,
970 Maizels RJ, Lauring J, Kriston-Vizi J, *et al* (2023) Active growth signaling promotes
971 senescence and cancer cell sensitivity to CDK7 inhibition. *Molecular Cell* 83: 4078-
972 4092.e6

973 Yang WS, SriRamaratnam R, Welsch ME, Shimada K, Skouta R, Viswanathan VS, Cheah JH,
974 Clemons PA, Shamji AF, Clish CB, *et al* (2014) Regulation of Ferroptotic Cancer Cell
975 Death by GPX4. *Cell* 156: 317–331

976 You DS, Bohrer CH, Rumde PH, Sanidas I, Swaffer MP, Larson DR, Elias JE, Lanz MC &
977 Skotheim JM (2025) Cell size-dependent mRNA transcription drives proteome
978 remodeling. 2025.10.30.685141 doi:10.1101/2025.10.30.685141 [PREPRINT]

979 Zatulovskiy E, Lanz MC, Zhang S, McCarthy F, Elias JE & Skotheim JM (2022) Delineation of
980 proteome changes driven by cell size and growth rate. *Front Cell Dev Biol* 10:
981 980721

982 Zatulovskiy E & Skotheim JM (2020) On the Molecular Mechanisms Regulating Animal Cell
983 Size Homeostasis. *Trends Genet* 36: 360–372

984 Zatulovskiy E, Zhang S, Berenson DF, Topacio BR & Skotheim JM (2020) Cell growth dilutes
985 the cell cycle inhibitor Rb to trigger cell division. *Science* 369: 466–471

986 Zhang N, Yu X, Song L, Xiao Z, Xie J & Xu H (2022a) Ferritin confers protection against iron-
987 mediated neurotoxicity and ferroptosis through iron chelating mechanisms in
988 MPP+-induced MES23.5 dopaminergic cells. *Free Radical Biology and Medicine*
989 193: 751–763

990 Zhang S, Valenzuela LF, Zatulovskiy E, Mangiante L, Curtis C & Skotheim JM (2024) The G1-S
991 transition is promoted by Rb degradation via the E3 ligase UBR5. *Science Advances*

992 Zhang S, Zatulovskiy E, Arand J, Sage J & Skotheim JM (2022b) The cell cycle inhibitor RB is
993 diluted in G1 and contributes to controlling cell size in the mouse liver. *Frontiers in*
994 *Cell and Developmental Biology* 10

995

996 **SUPPLEMENTARY DATA**

997
998

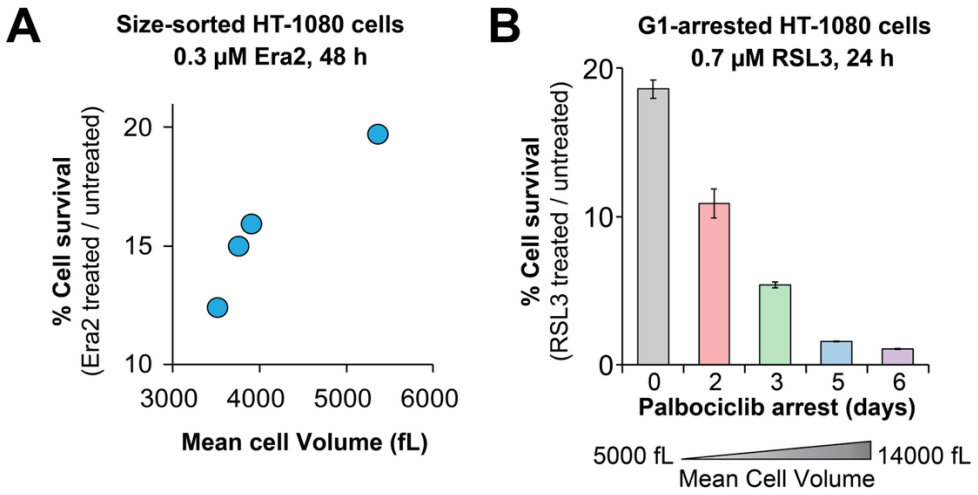

999
1000
1001 **Figure S1. Effects of cell size on Era2- and RSL3-induced ferroptosis susceptibility**
1002 **in HT-1080 cells.**
1003 (A) Cell survival percentage in HT-1080 cells sorted into four cell size bins using
1004 FACS. Cells were treated with 0.3 μM Era2 for 48 h, and cell survival percentage was calculated
1005 relative to DMSO-treated cells. The plot shows a representative example from *n* = 2 biological
1006 replicates. Each biological replicate included two technical replicates per condition, which were
1007 averaged for quantification of cell size and cell death sensitivity.
1008 (B) Cell survival percentage in HT-1080 cells whose size was increased through
1009 palbociclib-induced cell cycle arrest. After pre-treatment with palbociclib for the indicated numbers
1010 of days, the cells were exposed to 0.7 μM RSL3 in the presence of palbociclib for 24 h. Cell
1011 survival percentage was calculated relative to the cells treated only with palbociclib. Cell survival
1012 percentages are shown as means ± s.e.m.; n = 3 biological replicates.
1013

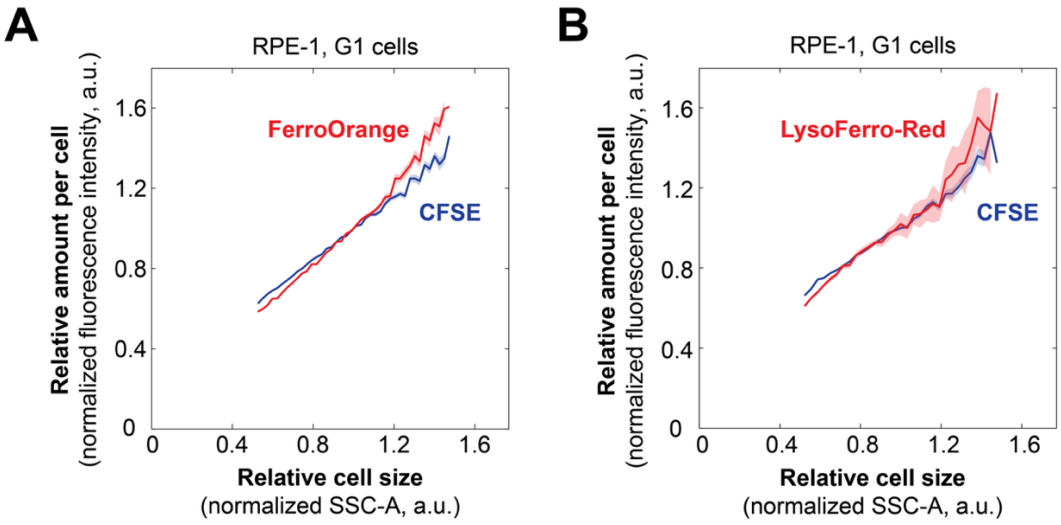

Figure S2. Cell size does not affect the concentrations of labile and lysosome-sequestered iron in RPE-1 cells.

(A,B) Flow-cytometry-based measurements of the amount of intracellular labile iron (A) and lysosome-sequestered iron (B) in G1-phase RPE-1 cells. Intracellular labile iron was detected with the FerroOrange fluorescent probe, and lysosomal iron was detected with the Lyso-FerroRed probe. Total cellular protein amount (CFSE staining), which scales in proportion to cell volume, is shown for reference. G1 cells were gated based on Hoechst DNA staining. The data were binned by cell size, and mean values for each bin were plotted against normalized cell size. Shaded areas denote the s.e.m. for each bin. Each sample included 100,000 cells.

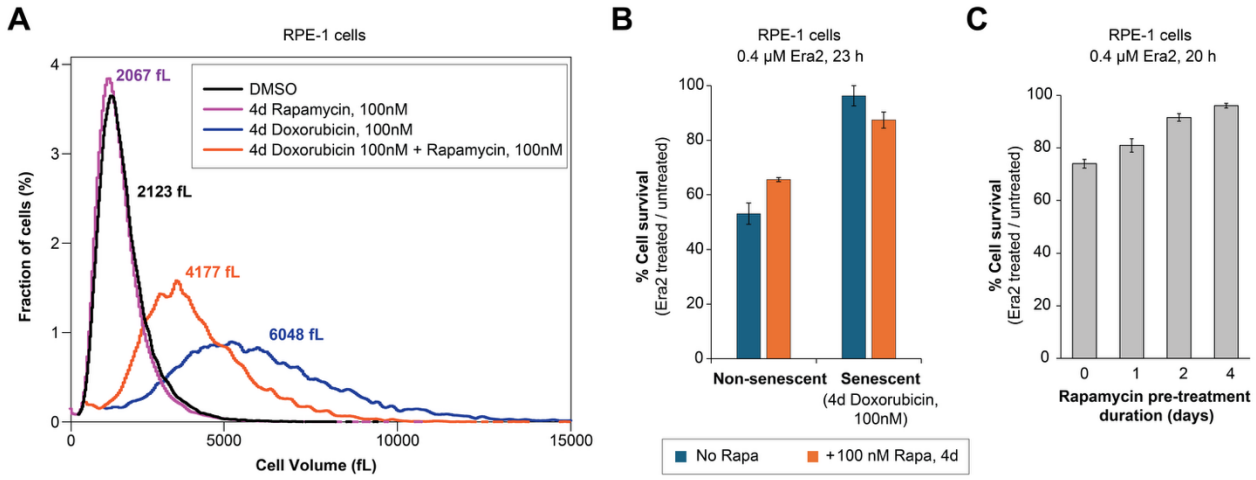

Figure S3. Senescent cells are large and resistant to Era2-induced ferroptosis.

(A) Cell size distributions of senescent and non-senescent (asynchronously proliferating) RPE-1 cells, measured with a Coulter counter. The numbers next to the histograms indicate mean cell size ± standard deviation for each condition. 4-day treatment with 100 nM doxorubicin was used to induce senescence in RPE-1 cells. To reduce the size of senescent cells, 100 nM of the mTORC1 inhibitor rapamycin was added to the media during the 4-day doxorubicin treatment.

(B) Cell survival percentage in senescent and non-senescent RPE-1 cells treated with 0.4 μM Era2 for 23 h. Senescent cells demonstrate significantly higher resistance to Era2 than non-senescent cells. Senescent cells pre-treated with rapamycin show only a modest reduction in cell survival. Cell survival percentage was calculated relative to the cells under the same conditions treated with DMSO instead of Era2. Error bars show s.e.m., n = 3 biological replicates.

(C) Prolonged cell pre-treatment with 100 nM mTORC1 inhibitor rapamycin causes a moderate decrease in cell sensitivity to Era2.

1042
1043
1044

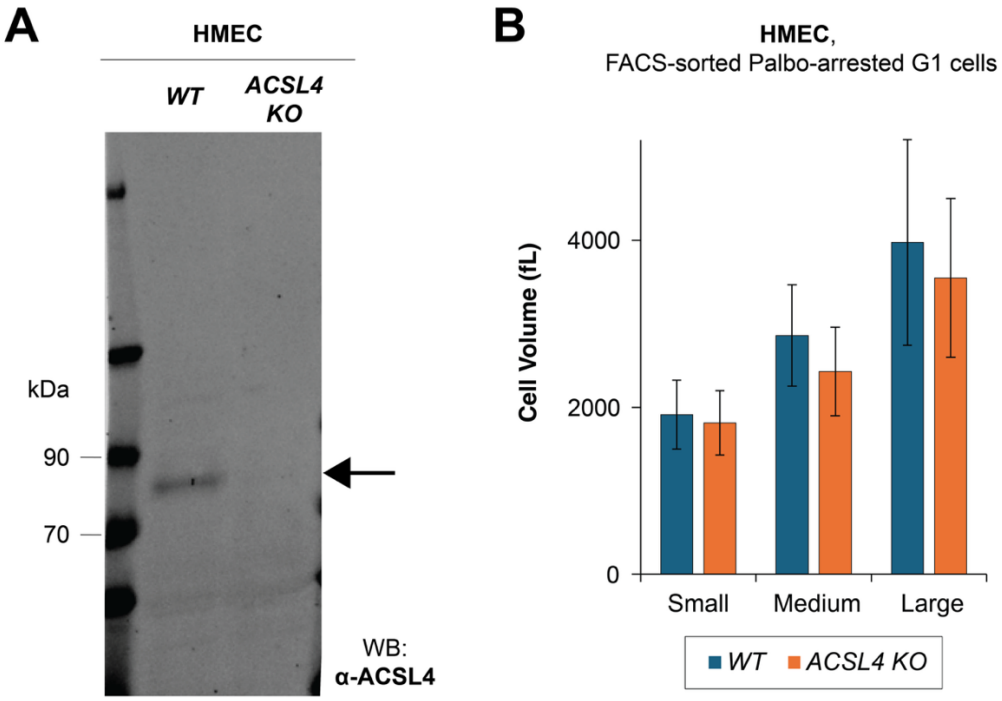

1045
1046
1047 **Figure S4. FACS-sorted *ACSL4 KO* HMEC cells have size distributions similar to**
1048 **those of *WT* HMEC cells.**
1049 (A) Validation of *ACSL4* knockout in HMEC cells with immunoblotting. Wild-type (*WT*) cell
1050 line and a mixed (not clonal) population of *ACSL4* knockout cells were analyzed using antibodies
1051 against ACSL4.
1052 (B) Mean cell sizes of small, medium, and large *WT* and *ACSL KO* HMEC cells after FACS
1053 sorting, measured on a Coulter counter. Error bars indicate cell size S.D. Prior to the sorting, the
1054 cells were synchronized in G1 phase by a 24 h treatment with 1 μM palbociclib.
1055

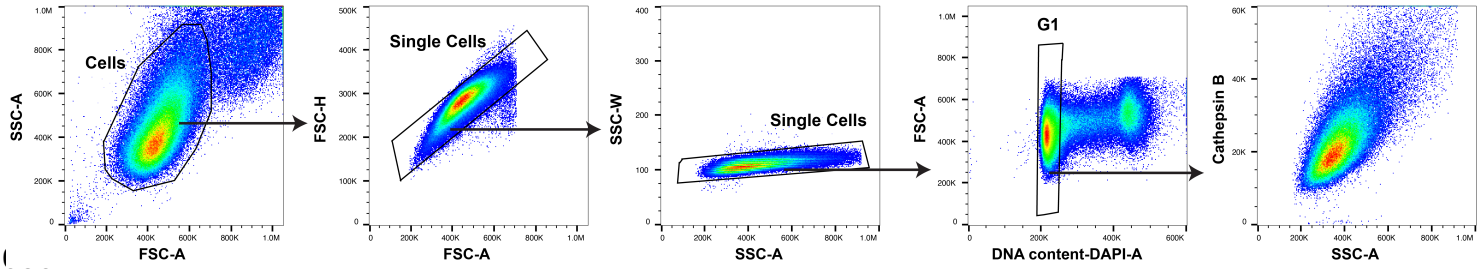

1057

1058 **Figure S5. Flow cytometry gating strategy for selecting G1 cells for subsequent**
1059 **scaling analysis.**

1060 Single cells were gated based on FSC-A vs SSC-A, then FSC-A vs FSC-H, then SSC-A
1061 vs SSC-W plots. From this population of single cells, G1 cells were selected using Hoechst-A vs
1062 FSC-A plot for subsequent scaling analysis (the example shown is for cathepsin B scaling
1063 analysis).